



A comprehensive investigation on the accuracy and efficiency of methods for melting temperature calculation using molecular dynamics simulations

Xinwei Wang, Mengxin Yang, Xiaoqian Gai, Yibo Sun, Bohan Cao, Jiajin Chen, Min Liang, Fubo Tian*, Liang Li*

State Key Laboratory of Superhard Materials, College of Physics, Jilin University, Changchun 130012, People's Republic of China



ARTICLE INFO

Keywords:

Melting temperature
Melting models
Crystal defects
Solid–liquid interfaces
Molecular dynamics simulations

ABSTRACT

Machine learning approaches have been extensively applied to improve the accuracy and reliability of potentials, addressing inherent limitations in molecular dynamics (MD) simulations. Notably, the precise determination of the melting temperature (T_m) relies on MD simulations, necessitating a comprehensive review of available melting models. This study aims to present a thorough comparison of various melting methods, including the single-phase method, hysteresis method, Z method, modified Z method, void method, modified void method, two-phase method, and sandwich method, considering both accuracy and efficiency. These melting models are systematically categorized into three groups: perfect crystals, crystal defects, and solid–liquid interfaces. The impact of factors such as atomic numbers, heating and cooling rates, crystal defects, and nucleation processes on T_m is discussed. Additionally, the temperatures corresponding to the superheating limit and the amorphous transition induced by heating and cooling rates during melting and crystallization processes are analyzed. Furthermore, the study explores the impact of different proportions of solid and the number of solid–liquid interfaces on melting behaviors. To further enhance the accuracy of T_m calculations, we propose a new approach termed the modified two-phase method, integrating the void method and two-phase method to account for crystal defects and solid–liquid coexistence, respectively.

1. Introduction

Melting is a topological transition from order to disorder, signifying the transformation of a crystal into a liquid [1–3]. High-pressure melting is fundamental for comprehending material properties under high temperatures and pressures [4–7]. It holds significant implications for constructing high-pressure equations of state in materials [4,7–10], allowing insights into the structure and variation of solid and liquid phases in the critical state [11]. Additionally, it finds applications in high-pressure science and deep geophysics [12–14]. However, a major challenge arises in achieving ultra-high pressures and temperatures simultaneously in experimental apparatus and in evaluating behavior during melting. Consequently, a substantial controversy persists regarding material melting at ultra-high pressures [12,15,16], fostering critical disagreements between high-pressure experimental techniques and theoretical simulations [12,15–17]. Consequently, the melting behavior of materials remains a vital scientific concern, extensively explored and pursued by researchers, regardless of iterative updates to

experimental apparatus or refinements in theoretical simulations [2,18–21].

On one hand, hydrostatic experimental techniques fail to emulate pressures and temperatures deep in the Earth. However, advancements in techniques [22,23] may pave the way for achieving higher pressures in the future [24]. On the other hand, dynamic high-pressure experiments offer the potential to measure the melting temperature (T_m) of materials at higher pressures [25,26], a critical range for modeling the deep interiors of planets [27]. Nevertheless, accurately measuring the internal T_m of an opaque material and evaluating its structure in a dynamic process with a short timescale remains exceptionally challenging [28]. Researchers have proposed various corresponding melting theoretical criteria, using lattice instability models [29–32], including the two-phase theory, Lindemann law, mechanical instability, thermoelastic instability, and defect melting criteria. Despite these efforts, none of these models proves universally applicable. Meanwhile, the Lindemann law [10,32,33], Simon–Glatzel law [13,34], Kraut–Kennedy equation [35], Wang's equation [36], and Clausius–Clapeyron law [37]

* Corresponding authors.

E-mail addresses: tianfb@jlu.edu.cn (F. Tian), liliang@jlu.edu.cn (L. Li).

are adopted to obtain melting curves for materials at high-pressure, facilitating reasonable extrapolations of T_m corresponding to those pressures. In the context of empirical melting theory, it can be concluded that melting is a bulk process resulting from lattice elastic instability or crystal defects, resulting in bulk melting at temperatures exceeding the thermodynamic temperature [12,38]. Experiments suggest that the melting process of crystals initiates at the crystal surfaces or with an inhomogeneous nucleation of the liquid in the inner interface, rather than being a bulk melting from the inside out [39].

Numerical simulation approaches serve as a powerful complement to traditional theoretical methodologies and experimental findings. They not only facilitate exploration of experimentally inaccessible and unobservable details, but also provide scientific predictions for traditional experiments [40–42]. Various simulation scales include First-Principles calculations, Molecular Dynamics (MD) simulations, Monte Carlo simulations, Phase Field, Rate Theory, and Finite Element methods. Among these, MD simulations enable the calculation of large-scale atomic systems, allowing observation of atomic dynamics and obtaining thermodynamic statistics, especially for high-pressure melting behaviors [2,3,11,12,18,20,43,44]. MD methods for simulating melting can be broadly categorized into direct and free energy approaches. Direct methods include the single-phase method [12,38,45,46], hysteresis method [45,47–49], Z method [2,3,44,50,51], modified Z method [2,3,44,51–56], void method [12,16,57,58], modified void method [59], two-phase method [3,12,60–66], and sandwich method [67,68]. Among these, the single-phase method, hysteresis method, and Z method determine T_m based on homogeneous nucleation theory. The modified Z method, void method, modified void method, two-phase method, and sandwich method reduce the free energy barrier to nucleation by creating voids or solid-liquid interfaces as defects in materials. These methods have successfully calculated the T_m of Mg [3], Ni and Pd [9], V [44], Al [53], Ta [54,56], Cu [55,59], and CaO [12,16], with the two-phase method extensively adopted for high-pressure melting and $P-T$ phase diagrams [3,12,69–74]. Furthermore, calculating the difference in free energy between the solid and liquid phases, along with determining the temperature and pressure conditions required for them to reach equilibrium, allows for a more accurate estimation of T_m , avoiding superheating effects. Considering this idea, several free energy approaches have been proposed [75–80], including the single-occupancy cell method of Hoover and Ree [75], the Einstein crystal method of Frenkel and Ladd [76], the λ -integral method [77], the pseudo-supercritical path method [78], and the interfacial pinning method [79,80]. Similarly, thermodynamic integration methods find wide application in studying melting temperatures and high-pressure melting curves [81–87]. Although these approaches have improved the accuracy of T_m , they are generally more complex and time-consuming than direct methods [53,59,88]. Various other methods for calculating T_m exist [70,89–93]. Recently, Ma *et al.* [94] and Cuong *et al.* [13] derived T_m directly from the equation of state parameters based on the work-heat equivalence principle, while Klimanova *et al.* [95] proposed that the T_m of materials can be accurately predicted through autonomous physics-informed learning.

In recent years, the development of machine learning potentials has overcome the limitations of previous empirical potentials, making a significant breakthrough in molecular dynamics (MD) research, particularly concerning melting and crystallization [96–103]. To deepen our comprehension of melting models, this study comprehensively compares the accuracy and efficiency of various methods, including the single-phase method, hysteresis method, Z method, modified Z method, void method, modified void method, two-phase method, sandwich method, and modified two-phase method. Additionally, the study explores the effects of atomic numbers, heating and cooling rates, crystal defects, different proportions of solid, and the number of solid-liquid interfaces on melting behaviors.

2. Theoretical models and computational methods

2.1. Melting models

Computational models for determining T_m using MD simulations include the single-phase method, hysteresis method, Z method, modified Z method, void method, modified void method, two-phase method, sandwich method, and modified two-phase method, as illustrated in Fig. 1. These MD simulation-based melting models can be categorized into three groups: perfect crystals, crystal defects, and solid-liquid interfaces. Among these, the hysteresis method, Z method, and void method are models proposed to eliminate the superheating effect observed in the single-phase method, essentially representing variations of a single-phase method. The modified Z method, modified void method, two-phase method, sandwich method, and modified two-phase method are grounded in the theory of solid-liquid coexistence and the calculated results yield highly accurate.

2.1.1. Single-phase method

The single-phase method [12,38,46,75] is a commonly employed approach for calculating T_m of materials. In this method, materials undergo uniform heating at a fixed pressure and a rate of increase (10^{11} – 10^{14} K/s) until complete melting occurs. During the heating process, atoms adjust their positions through movement while the system maintains a certain temperature, resulting in a decrease in energy. Once structural relaxation reaches equilibrium at this temperature, atoms thermally vibrate around their equilibrium positions. Beyond T_m , the atomic structure tends toward a disordered state, considered as T_m . Higher values than experimental T_m are attributed to the use of a perfect crystal as the initial model in the single-phase approach, neglecting factors enabling inhomogeneous nucleation [12]. Moreover, the limited number of atoms in the system and the rapid heating rates contribute to a high degree of superheating, typically around 10–35 % [44]. Consequently, accurately determining the extent of superheating in a system is challenging. To thoroughly investigate the process simulated by the single-phase method, the employed melting models include a cubic, a cuboid, and a sphere models, each with the addition of a vacuum layer [104]. The calculation models are illustrated in Fig. 2(a)–(f).

2.1.2. Hysteresis method

The single-phase method induces superheating during the melting process, and similarly it leads to supercooling to a similar degree when adopted to simulate liquid crystallization. Consequently, the heating and cooling processes in the single-phase method result in a superheating temperature (T_+) and a supercooling temperature (T_-) for T_m . Ultimately, a closed loop is formed on the volume-temperature ($V-T$) curves, allowing for the averaging of the superheating and supercooling, thus enabling the empirical calculation of T_m . This approach is known as the hysteresis method [45,47–49]. Fig. 3(a) and (b) provide an overview of possible states during heating and cooling processes: a solid solution and a liquid, an amorphous and a crystal, but they are also inherently a single-phase method in nature. Luo *et al.* [47] derived an empirical formula for calculating T_m from the superheating and supercooling temperatures using the homogeneous melting theory, i.e., T_m is defined as

$$T_m = T_+ + T_- - \sqrt{T_+ T_-}, \quad (1)$$

Although this approach reduces the problem of superheating to a certain extent, it lacks a physical context. Moreover, the heated crystal forms a melt due to the temperature being slightly above the actual T_m , as depicted in Fig. 3(a). Similarly, the cooled liquid may crystallize into a solid different from the initial state, exhibiting an amorphous structure, as shown in Fig. 3(b). All these states can significantly impact the estimation of T_m in the hysteresis method [44,53].

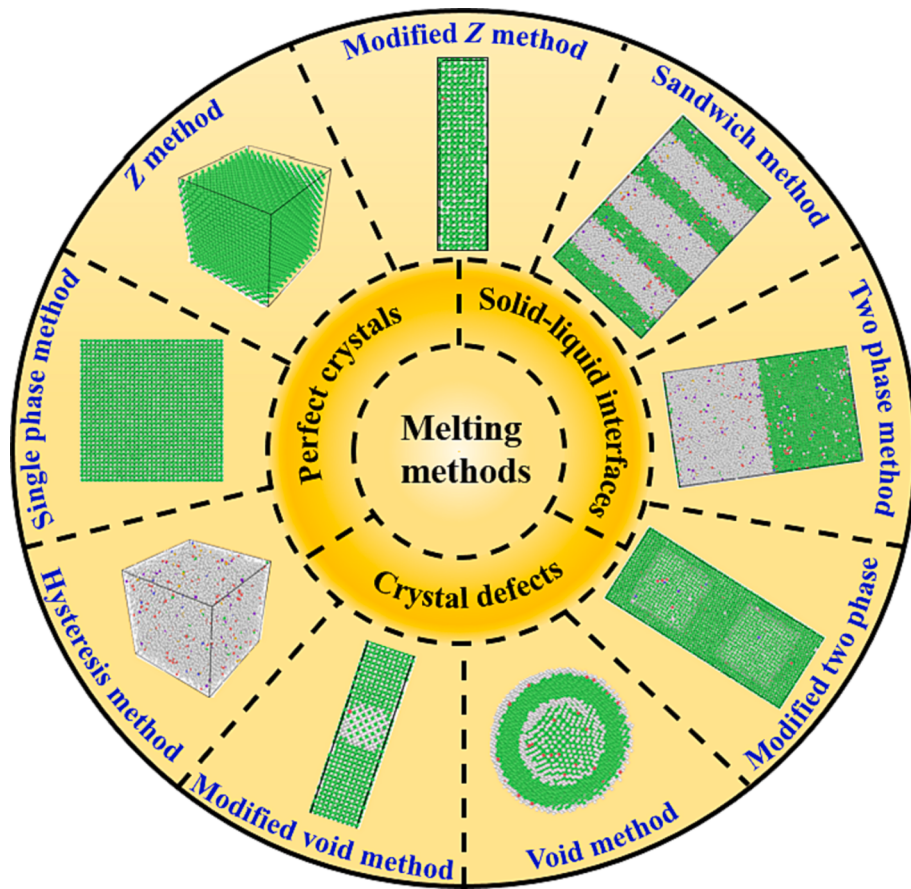


Fig. 1. MD methods are applied to simulate the melting temperature, including the single-phase method, hysteresis method, Z method, modified Z method, void method, modified void method, two-phase method, sandwich method, and modified two-phase method.

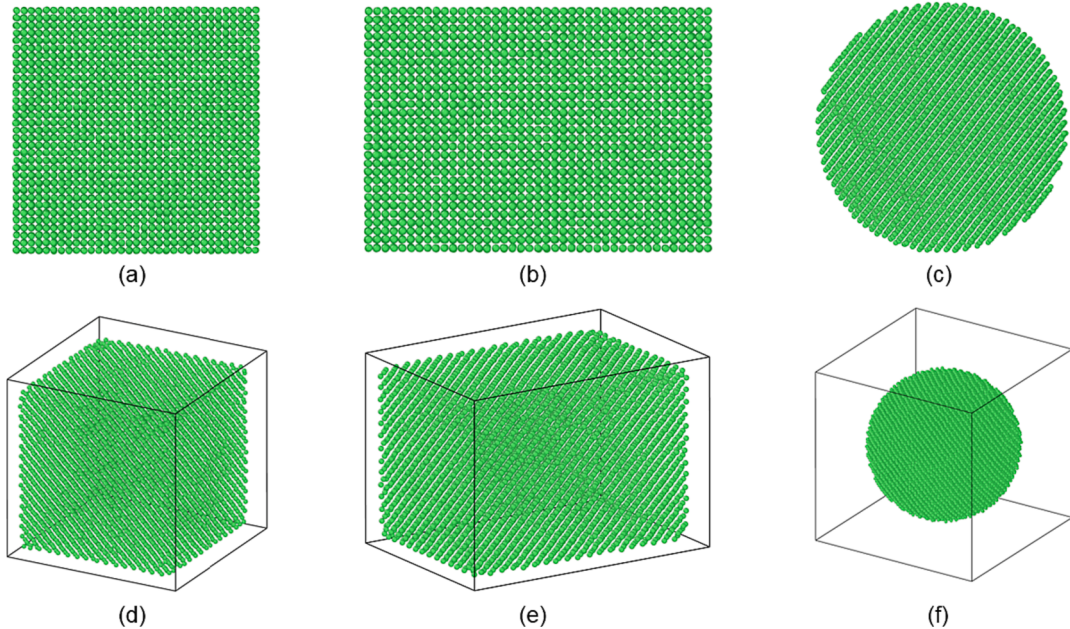


Fig. 2. In the simulation for single-phase method, the calculation models of the melting temperature include (a) a cubic, (b) a cuboid, (c) a sphere, as well as with the addition of a vacuum layer for (d) a cubic, (e) a cuboid, and (f) a sphere.

2.1.3. Z method

Belonoshko *et al.* [51] proposed the Z method based on the physical idea that atoms can spontaneously reach equilibrium. Simulations are

performed in a fixed-volume model with a high initial temperature applied to perfect crystals in a microcanonical (NVE) ensemble for a significant duration [2,3,44,50]. Throughout the heating process, atoms

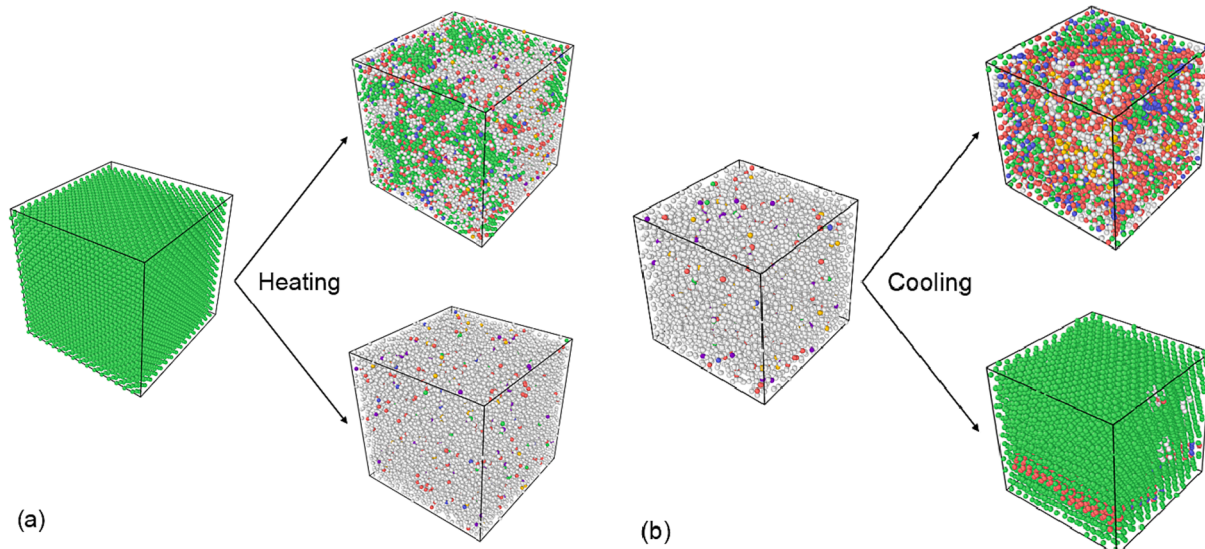


Fig. 3. Possible states of Cu atoms during heating and cooling processes are (a) a crystal with increasing temperature, ultimately heated as a solid solution or a liquid, and (b) a liquid with decreasing temperature, ultimately cooled as an amorphous or a crystal. In subsequent figures in this work, atoms are color-coded in green for FCC, red for HCP, blue for BCC, purple for SC, yellow for ICO, and white for Other clusters. (For interpretation of the references to color in this figure legend, the reader is referred to the web version of this article.)

gain the ability to cross lattice barriers and break free from lattice constraints, diffusing into the surrounding area, causing the volume to expand, and leading to an increase in pressure with temperature. At the moment of melting, the temperature of the system drops rapidly due to heat absorption, while the pressure continues to increase due to volume expansion. **Fig. 4** illustrates the potential states of the Z method during the heating process, representing a solid and a liquid. Generally, the Z

method adopts the minimum temperature of the liquid in the P - T relationships as T_m [44,50]. Despite its extensive use in *ab initio* MD (AIMD) investigations of melting for various materials due to its simplicity and suitability for small systems [2,3,44], later findings reveal numerous counterexamples [105], indicating that the Z method is no better than the single-phase method, which also provides only an upper limit T_+ for T_m .

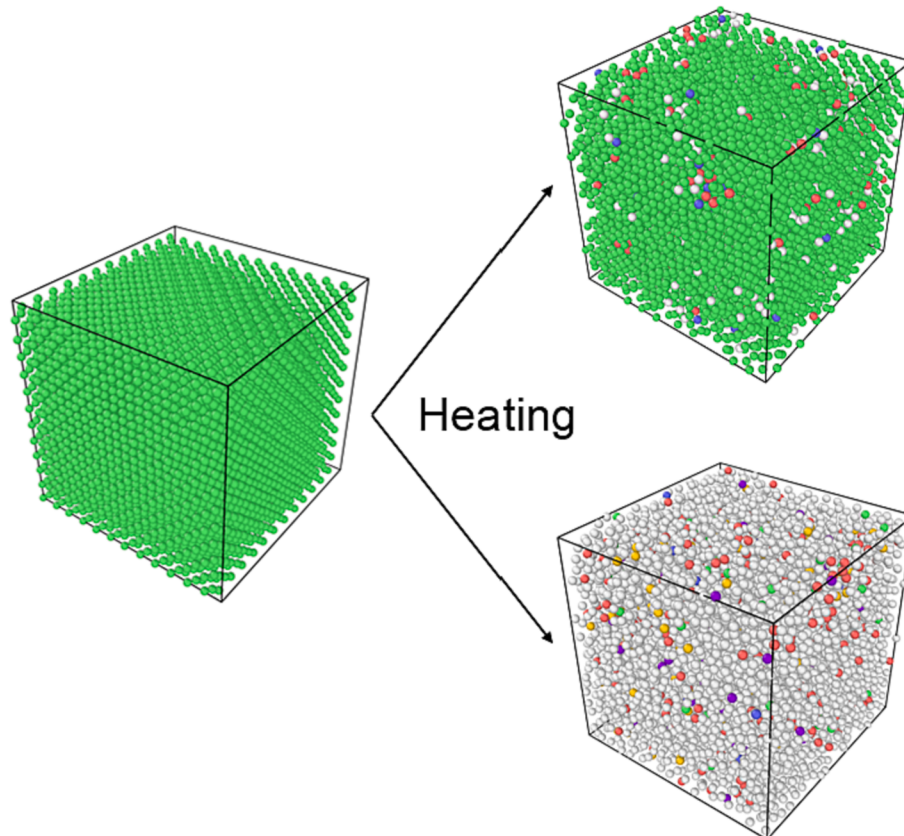


Fig. 4. Potential states of Cu atoms include a solid and a liquid with increasing temperature in the Z method.

2.1.4. Modified Z method

The Z method has undergone further development, leading to the proposal of a modified Z method by Wang *et al.* [55]. Fig. 5(a)–(c) presents the states that can occur during the simulation of the modified Z method, including a solid, a liquid, and a solid–liquid coexistence. Based on the Z method the cubic is replaced with a cuboid model in the modified Z method, with the length in the z direction greater than the x and y directions to achieve stable solid–liquid coexistence [52–54,56]. The introduction of this coexistence state not only avoids superheating effects but also provides a clearer physical definition of the modified Z method. The initial temperature is set around the predicted T_m in the modified Z method [53,55]. Although the modified Z method combines the inherent simplicity of the Z method with the advantages of its coexistence state, it results in a coexistence state that is not in hydrostatic equilibrium. To achieve equilibrium under hydrostatic pressure, Karavaev *et al.* [53] simulated the stresses in the equilibrium system without changing its volume, and their results demonstrated that the stresses calculated by the modified Z method are balanced and as accurate as those obtained by the thermodynamic integration method. Additionally, the T_m obtained using the modified Z method strongly depends on the relaxation time, and melting fails to occur when the relaxation time for the system is short [55].

2.1.5. Void method

The void method is designed to eliminate the superheating caused by the single-phase method [12,16,57,58,106], as illustrated in Fig. 6(a)–(d). Fig. 6(a) illustrates the creation of cubic defects in a cubic model (referred to as Model I). The void method reduces superheating by introducing a crystal defect. In actual material environments, the periodic arrangement of atoms leads to inevitable defects, rendering melting processes varied and complex. Concrete manifestations of these phenomena include superheating and pre-melting. The presence of defects significantly enhances the diffusion ability of atoms, increasing the energy of the system and lowering the energy barrier for nucleation in the liquid phase, thereby thermodynamically promoting nucleation. Mechanistically, defects provide favorable conditions for the formation and growth of the liquid, with melting typically initiating in the vicinity of the defects [12,106]. The simulation process involves creating a cube model with defects, heating the system to melting under an isothermal-isobaric (NPT) ensemble and monitoring the variation of atomic volume with temperature. Considering the atomic number of defects, the final estimate of T_m is obtained where the equilibrium temperature T_b of each system stabilizes with increasing defects. Furthermore, Joshi *et al.* [104] proposed the spherical shell model (referred to as Model II), as plotted in Fig. 6(b), which is similar in principle to the void method as both consider defects within the crystal. Two methods of creating defects are also proposed: the creation of spherical defects in the cubic model (referred to as Model III), as depicted in Fig. 6(c), and the random deletion of atoms in the cubic (referred to as Model IV), as plotted in Fig. 6(d).

2.1.6. Modified void method

The void method utilizes crystal defects, and its simulated T_m reduces the issue of superheating to some extent. However, it falls short of incorporating the solid–liquid coexistence theory. To address this, a modified void method proposed by Zou *et al.* [59], based on inhomogeneous nucleation, efficiently calculates the T_m of the material as displayed in Fig. 7. The efficiency in calculating T_m compared to the void method is attributed to the use of defects, which reduces free energy barriers and allows for the rapid formation of a liquid nucleus, achieving a stable solid–liquid coexistence. In comparison to the two-phase method, it maintains identical accuracy but is more computationally efficient [59]. The initial model for the modified void method is a cuboid and the simulation process involves three steps: first, simulating a perfect crystal in the isobaric–isoenthalpic (*NPH*) ensemble until equilibrium at a given temperature. The second step is creating a cubic defect. Finally, the system with cubic defects is continuously simulated in the *NPH* ensemble to achieve equilibrium. A stable solid–liquid coexistence state is attained at the appropriate enthalpy of the system.

2.1.7. Two-phase method

Traditionally, T_m is usually performed by determining the Gibbs free energy of the solid and liquid phases, allowing for the direct determination of the melting curve. However, calculating the free energy is a non-trivial task [107,108]. Another approach involves simulating the coexistence of the two phases [69,109–112], enabling the direct calculation of the equilibrium T_m . The procedure entails initially constructing a perfect crystal structure for Cu atoms. The positions of atoms in one-half of the system are fixed, while the other half is heated to a high temperature for an extended period to ensure the complete melting of the unfixed atoms. Subsequently, the heated atoms are rapidly cooled to a temperature slightly above the melting temperature for a brief period. Finally, the fixed atoms are released, fixing the other half in parallel. The temperature is gradually increased to the predicted T_m , achieving a solid–liquid coexistence initial configuration for each half. Commonly applied ensembles for the two-phase method include *NPT* [88,93], *NVE* [60,71,73], *NPH* [109], *NPT–NVE* [12,63,66], *NVE–NPH* [59], *NVT–NPT* [75], *NVT–NPT–NPH* [74], *NVT–NVE* [110]. In the present work, the two-phase method, the sandwich method, and the modified two-phase method all adopt the *NPT* and *NVE* ensembles. Fig. 8(a)–(c) illustrate the three initial models considered in our study, with 25 %, 50 %, and 75 % solid atoms, respectively.

2.1.8. Sandwich method

In contrast to the atoms inside pure solids and liquids on either side, the atoms located in the transition region are influenced by the combined action of the solid and liquid phases. Therefore, the structure of the solid–liquid interface is therefore distinctly different from the structure of the solid and liquid interiors. Fig. 9(a)–(c) illustrate the initial models for the sandwich method in the present work [67,68], depicting two, four, and six solid–liquid interfaces, respectively. As an

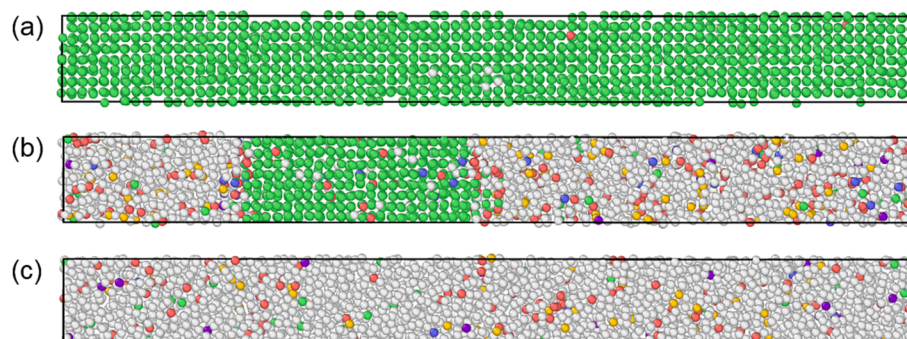


Fig. 5. Potential states of Cu atoms with increasing temperature in the modified Z method include (a) a solid, (b) solid–liquid coexistence, and (c) a liquid.

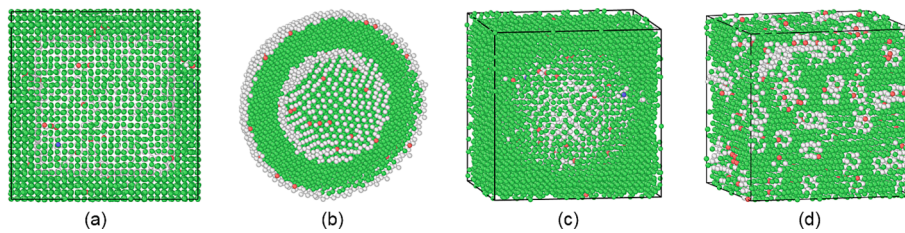


Fig. 6. Initial models applied in the void method include (a) a cubic defect in a cubic model (Model I), (b) a spherical shell model (Model II), (c) a sphere defect in a cubic model (Model III), and (d) a random deletion of the number of atoms in a cubic model (Model IV).

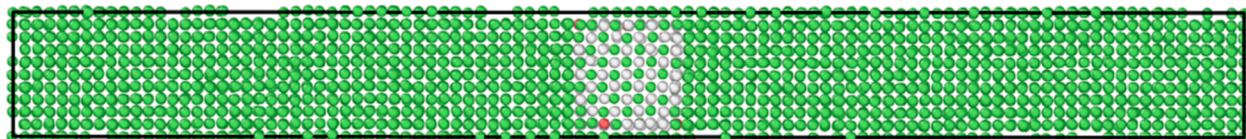


Fig. 7. A cubic defect is introduced in the cuboid as the initial model for the simulation in the modified void method.

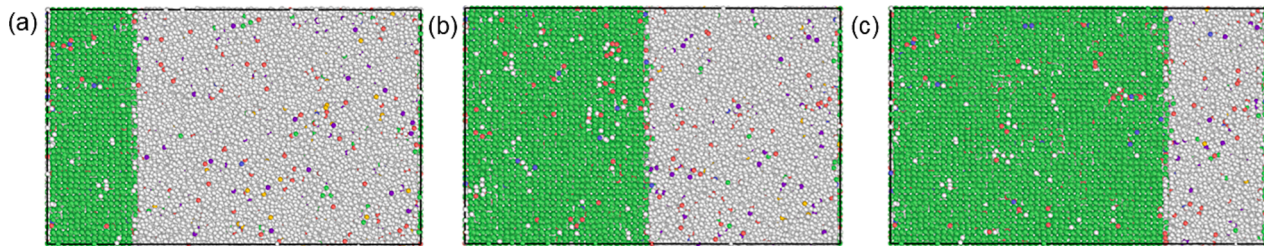


Fig. 8. Initial models for the two-phase method include (a) a 25% solid atom, (b) a 50% solid atom, and (c) a 75% solid atom.

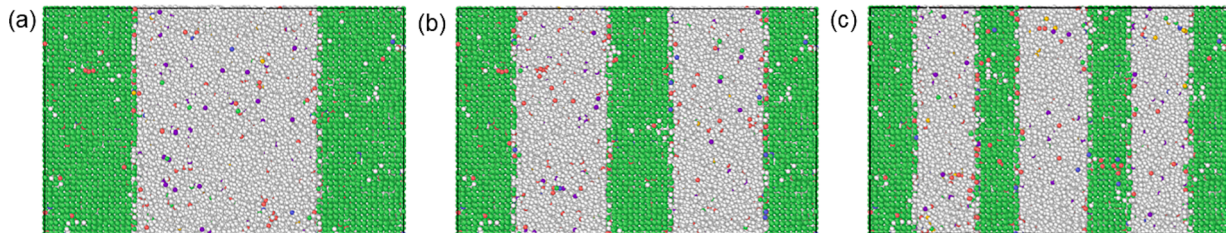


Fig. 9. Initial models for the sandwich method include (a) two solid–liquid interfaces, (b) four solid–liquid interfaces, and (c) six solid–liquid interfaces.

example, the initial model with two interfaces applies periodic boundary conditions in the x , y , and z directions and constructs alternating liquid–solid layers in the z direction. This means that the model has 1/2 solid on each side and 1/2 liquid in the middle. Two solid phases and one liquid phase are independently equilibrated at two different temperatures. After reaching equilibrium all atoms run within the NPT ensemble at a certain temperature and the behavior of the system is observed. If a solid–liquid coexistence transitions into a homogeneous liquid, the temperature is above T_m , and conversely, it is below T_m .

2.1.9. Modified two-phase method

The two-phase method is acknowledged for its accurate calculation of T_m with a clear physical definition. While effective in reducing superheating, the void method considers defects in the material, but the impact of defects on T_m is not adequately addressed [106]. The initial structure of the two-phase method is a perfect lattice, lacking consideration for crystal defects [12]. To enhance the accuracy of T_m determination in the melting process, we propose a new approach that combines the void method and the two-phase method, termed the modified two-phase method. This method is fundamentally grounded in the theory of solid–liquid coexistence and incorporates crystal defects,

bringing the melting model closer to the real existing state. The simulation process involves constructing a perfect lattice of a cubic, relaxing all the atoms at 300 K in the NPT ensemble to eliminate stresses among atoms. Second, Fig. 10(a) and (b) give the initial structure of the modified two-phase method by splitting the simulated system in two and creating a cubic defect in the center of each half. Third, one half of the atoms are fixed while the other half is heated to a higher temperature, and the equilibrium needs to be timed to ensure that the heated atoms are completely melted. Finally, the fixed atoms are released and the whole system evolves under the NPT ensemble.

2.2. Simulation methods

The LAMMPS software package [113] is adopted in MD simulations for constructing the initial configuration of Cu atoms and calculating the T_m along with related properties. The experimental lattice constant for Cu is 3.615 Å [114], with x , y , and z corresponding to [100], [010], and [001] orientations, respectively. To eliminate the effects of surfaces and defects, a periodic boundary condition is applied in the x , y , and z directions. Other simulation conditions match those in the Ref. [59]. Time steps of 1 fs are selected and data such as temperature, energy, volume,

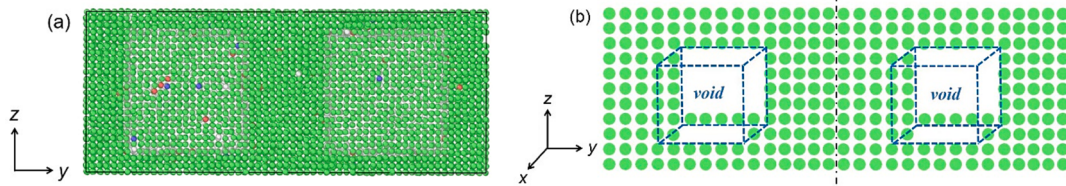


Fig. 10. Modified two-phase model with cubic defects created on each side of the simulated system, where (a) is a two-dimensional plane, and (b) is a three-dimensional diagram.

and positions are output. Atomic trajectories are visualized using OVITO [115]. For the Z method, modified Z method, and modified void method, the simulation time is 2 ns at each temperature and the last 0.5 ns of output data are analyzed. For the void method, a different system with a heating rate of 1×10^{12} K/s is adopted. For the two-phase method, sandwich method, and modified two-phase method, the simulation time is 1–2 ns at each temperature. The interaction among Cu atoms is

described by the Embedded Atom Method (EAM) proposed by Mishin *et al.* [114]. The total potential energy of the crystal within the EAM potentials can be expressed as:

$$U(r_{ij}) = \sum_i F_i(\rho_i) + \frac{1}{2} \sum_{j \neq i} \phi_{ij}(r_{ij}), \quad (2)$$

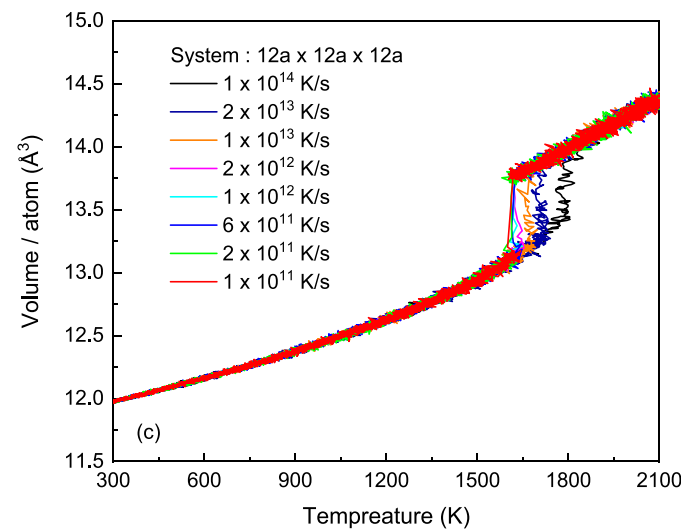
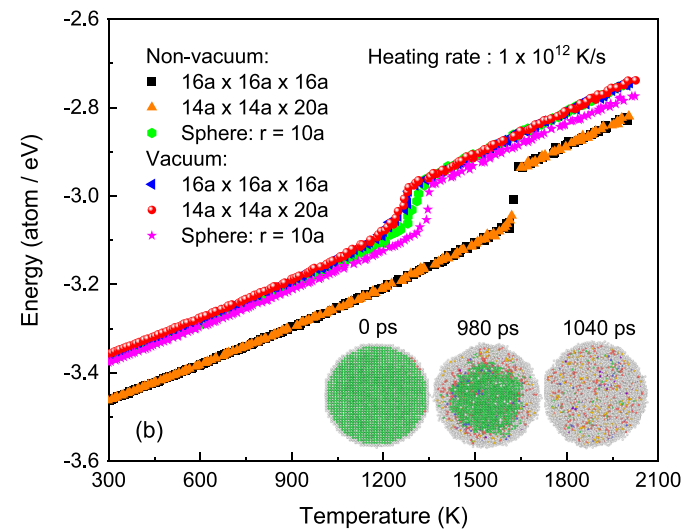
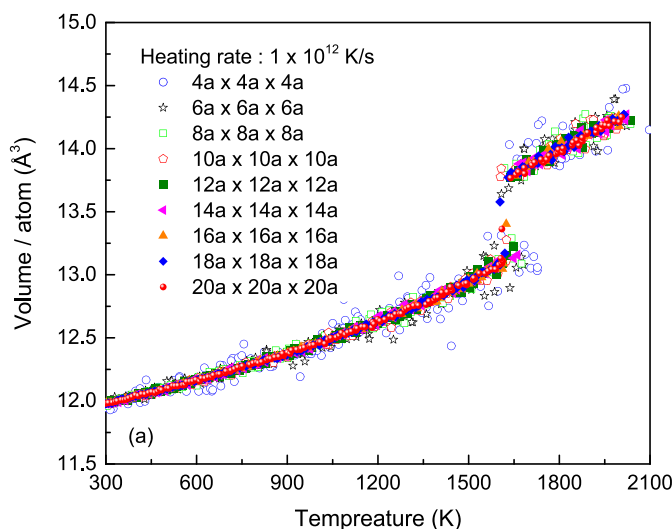


Fig. 11. Variation in the melting temperature of Cu atoms due to different atomic numbers in the system, different heating rates, and different melting models: (a) atomic numbers ranging from $4a \times 4a \times 4a$ to $20a \times 20a \times 20a$ in the cubic system, (b) melting models including non-vacuum and vacuum layers for the cubic, cuboid, and sphere, with the interpolated atomic structures of the sphere corresponding to simulation times of 0, 980, and 1040 ps, respectively, and (c) heating rates ranging from 1×10^{11} K/s to 1×10^{14} K/s for the system of $12a \times 12a \times 12a$.

where the first term F_i represents the embedding energy and the second term is the pair potential term. ρ_i represents the sum of the electron cloud densities produced at the i th atom by the out-of-nuclear electrons of all but the i th atom, which can be expressed as:

$$\rho_i = \sum_{j \neq i} f_j(r_{ij}), \quad (3)$$

where $f_j(r_{ij})$ represents the charge density contributed by the out-of-nuclear electrons of the j th atom at the i th, and r_{ij} represents the distance between the i th atom and the j th.

3. Results and discussion

3.1. Melting temperature from single-phase method

To investigate the effect of atomic number on the system and different heating rates on T_m , MD simulations are performed using a single-phase method with the NPT and NVT ensembles. On one hand, Cu atoms are placed in systems ranging from $4a \times 4a \times 4a$ to $20a \times 20a \times 20a$ at a heating rate of 1×10^{12} K/s. On the other hand, the heating rates are from 1×10^{11} K/s to 1×10^{14} K/s for a system of $12a \times 12a \times 12a$. The temperature ranges from 300 K to 2000 K, with data output for temperature, volume, and energy every 100 K intervals. Fig. 11(a)–(c) provide the T_m of Cu atoms due to different numbers of atoms, heating rates, and melting models, respectively. In Fig. 11(a), the T_m obtained for systems from $4a \times 4a \times 4a$ to $20a \times 20a \times 20a$ are presented in Table 1. During the melting process, changes in energy and volume lead to variations in atomic structure. The average kinetic energy of atoms gradually increases with temperature, resulting in a higher probability of atomic collisions. Moreover, with the increase in volume and irregular thermal motion of atoms, the relative positions of atoms change constantly, affecting the potential energy. The energy reaches a peak when temperature and volume fluctuations reach T_m [104]. The impact of similar atomic numbers on T_m is weak, as seen in Table 1, indicating that the size effect can be neglected for a range of atomic numbers [12]. Superheating in this work ranges from 18 % to 27 %. However, the V-T curves in Fig. 11(a) reveal that the larger the number of atoms in the system, the smaller the vibrational amplitude of atomic volume, as central atoms are more constrained by their surroundings. The phenomenon also indicates that the periodic system has relatively sufficient time for atoms to achieve a metastable or stable state at a heating rate of 1×10^{12} K/s [12,16,38,59,116].

Fig. 11(b) presents simulation results for a cubic model ($16a \times 16a \times 16a$), a cuboid model ($14a \times 14a \times 20a$), a sphere model ($r = 10a$) and three models with a vacuum layer of 10 Å. The obtained T_m for the $16a \times 16a \times 16a$ and $14a \times 14a \times 20a$ are 1613 K and 1615 K respectively, illustrating a relatively small difference between the results for cubic and cuboid models. Simulations with the addition of a vacuum layer at 1242 K for the $16a \times 16a \times 16a$ and $14a \times 14a \times 20a$ respectively, indicate a significant difference in T_m between simulations with and without the addition of vacuum layers [104]. The application of periodic boundary conditions and vacuum layers in the simulation leads to the

formation of the free surface of the crystal [104]. Bonds of atoms on the surface break as the crystal forms a surface, distinct from atoms inside the crystal. Surface atoms are only partially connected with other atoms and have fewer neighboring atoms than those inside the crystal, resulting in a surface with higher energy than internal atoms. Consequently, the overall energy is higher than without the addition of a vacuum layer, consistent with the phenomenon depicted in Fig. 11(b). Meanwhile, the simulation results are consistent for both the cubic and cuboid models, making them applicable as initial models for the single-phase approach. The calculated results of 1285 K and 1306 K for a sphere model with a vacuum layer and a sphere model are below the experimental result of 1358 K [117] and significantly differ from the results for cubic and cuboid models. The E-T curves for the spheres in Fig. 11(b) reveal that the energy per-atom is higher than for both the cubic and cuboid models, revealing that the atomic structure in the sphere is not as stable as in the cubic and cuboid models.

The magnitude of the heating rate during the melting process directly influences the degree of ordering for atoms at the same temperature [59,118,119]. Fig. 11(c) illustrates the variation of volume with temperature for an atomic system of $12a \times 12a \times 12a$ and heating rates from 1×10^{11} K/s to 1×10^{14} K/s, with T_m values presented in Table 2. Higher heating rates lead to higher T_m values because atoms fail to reach a stable kinetic and thermodynamic equilibrium within a remarkably short period due to rapid heating [59,118,119]. Additionally, with a smaller rate of temperature increase, the atoms within the system are heated more homogeneously. The overall order of the atoms at each temperature is higher, and the system exhibits stronger global convergence [38]. Consequently, the phase transition due to the continued change in temperature and volume becomes more intense as the heating approaches T_m . Correspondingly, the duration of the structural transition process is relatively short [38,59]. As the heating rate increases, the T_m of the system significantly rises, and the energy required for melting to occur at the starting temperature range decreases. There is no significant jump in the E-T curves at 1780 K when the heating rate reaches 1×10^{14} K/s, as plotted in Fig. 11(c). Once the heating rate reaches a certain value, the energy required for melting at 1780 K is already quite small, and the corresponding temperature is the stable limit for the superheating of a perfect crystal. The reason is that as the temperature increases, the random motion of the atoms in the system increases, leading to increased atomic disorder. At the high heating rates, the system cannot reach equilibrium at a certain temperature, resulting in the occurrence of superheating. Simultaneously, the high degree of internal atomic disorder and increased random motion increase the energy of the system, reducing the energy required for melting to occur. This results in a kinetically stable limit temperature for the superheating phenomenon caused by the heating rates, illustrating that the superheating limit for Cu in our work is 1780 K. Since the system is a perfect crystal, the obtained superheating limit is higher. Furthermore, the heating rate directly influences the temperature interval over which the energy increases sharply with time during the melting processes, as seen in Fig. 11(c). The temperature interval $\Delta T = 5$ K for the energy surge at a rate of 1×10^{11} K/s, $\Delta T = 12$ K at a rate of 1×10^{12} K/s, and $\Delta T = 32$ K at a rate of 1×10^{13} K/s. As the heating rate increases,

Table 1

Comparison of the effect on the melting temperature of the simulated systems ranging from $4a \times 4a \times 4a$ to $20a \times 20a \times 20a$ at a heating rate of 1×10^{12} K/s, with the number of atoms in the corresponding system in parentheses.

Systems	T_m (K)	System	T_m (K)
$4a \times 4a \times 4a$ (256)	1724 ± 10	$11a \times 11a \times 11a$ (5324)	1631 ± 10
$5a \times 5a \times 6a$ (500)	1677 ± 10	$12a \times 12a \times 12a$ (6912)	1626 ± 10
$6a \times 6a \times 6a$ (864)	1675 ± 10	$13a \times 13a \times 13a$ (8788)	1631 ± 10
$7a \times 7a \times 7a$ (1372)	1683 ± 10	$14a \times 14a \times 14a$ (10976)	1634 ± 10
$8a \times 8a \times 8a$ (2048)	1649 ± 10	$16a \times 16a \times 16a$ (16384)	1613 ± 10
$9a \times 9a \times 9a$ (2916)	1639 ± 10	$18a \times 18a \times 18a$ (23328)	1610 ± 10
$10a \times 10a \times 10a$ (4000)	1628 ± 10	$20a \times 20a \times 20a$ (32000)	1605 ± 10

Table 2

Comparison of the effect of heating rates ranging from 1×10^{14} K/s to 1×10^{11} K/s on the melting temperature for a system of $12a \times 12a \times 12a$.

Systems	Rate (K/s)	T_m (K)
$12a \times 12a \times 12a$ (6912)	1×10^{14}	1780 ± 10
	2×10^{13}	1711 ± 10
	1×10^{13}	1664 ± 10
	2×10^{12}	1631 ± 10
	1×10^{12}	1626 ± 10
	6×10^{11}	1610 ± 10
	2×10^{11}	1608 ± 10
	1×10^{11}	1605 ± 10

the required temperature difference for the melting process also increases, consistent with the theory of molecular thermal motion.

3.2. Melting temperature from hysteresis method

Fig. 12(a) provides the effect on the superheating and supercooling curves for the systems ranging from $12a \times 12a \times 12a$ to $14a \times 14a \times 20a$ at heating and cooling rates of 1×10^{12} K/s. The T_m values obtained at a heating rate of 1×10^{12} K/s are in the range of 1600–1650 K, as presented in **Table 3**. The effect of heating and cooling rates from 5×10^{11} K/s to 1×10^{13} K/s on the superheating and supercooling curves is investigated in **Fig. 12(b)** for a system of $12a \times 12a \times 12a$. The stability of superheating crystals tends to decrease as the heating rate increases. Non-equilibrium heating processes at high heating rates cause significant disruption of the periodic structure within the crystal, dramatically reducing the phase transition barrier of the superheating crystal and promoting nucleation of the liquid phase. The effect of heating rates on the superheating and melting behavior of superheating crystals is reflected in the observation that higher heating rates result in higher T_m values [59,116].

The supercooling curves for Cu atoms are described in **Fig. 12(a)** and (b), showing that the number of atoms in the system has little effect on supercooling. The impact of high cooling rates is most significant,

Table 3

Hysteresis method provides simulation results for the cubic model, the cuboid model, and different heating and cooling rates to obtain the melting and crystallization temperatures, with the number of atoms in the corresponding system in parentheses.

Systems	Rate (K/s)	T_+ (K)	T_- (K)	T_m (K)
Cubic module				
$12a \times 12a \times 12a$ (6912)	1×10^{12}	1611–1628	771–823	1278–1283
$14a \times 14a \times 14a$ (10976)	1×10^{12}	1609–1628	724–795	1266–1273
$16a \times 16a \times 16a$ (16384)	1×10^{12}	1608–1615	768–795	1269–1272
Cuboid module				
$10a \times 10a \times 16a$ (6400)	1×10^{12}	1609–1628	727–795	1267–1273
$12a \times 12a \times 18a$ (10368)	1×10^{12}	1609–1625	733–790	1266–1271
$14a \times 14a \times 20a$ (15680)	1×10^{12}	1609–1628	771–795	1273–1278
Different rate				
$12a \times 12a \times 12a$ (6912)	5×10^{11}	1609–1619	798–839	1280–1286
$12a \times 12a \times 12a$	1×10^{12}	1611–1628	771–823	1278–1283
$12a \times 12a \times 12a$	2×10^{12}	1619–1638	749–790	1273–1278
$12a \times 12a \times 12a$	5×10^{12}	1630–1652	590–620	1245–1255
$12a \times 12a \times 12a$	1×10^{13}	1622–1638	—	—

contributing to greater superheating in the system [59,116]. The variation of the average atomic volume of the system with temperature at a cooling rate of 1×10^{13} K/s is continuous and indicates a secondary phase transition, signifying an amorphous transition of the system

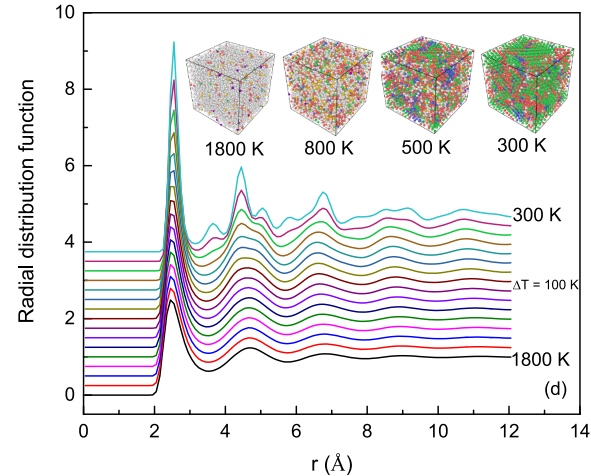
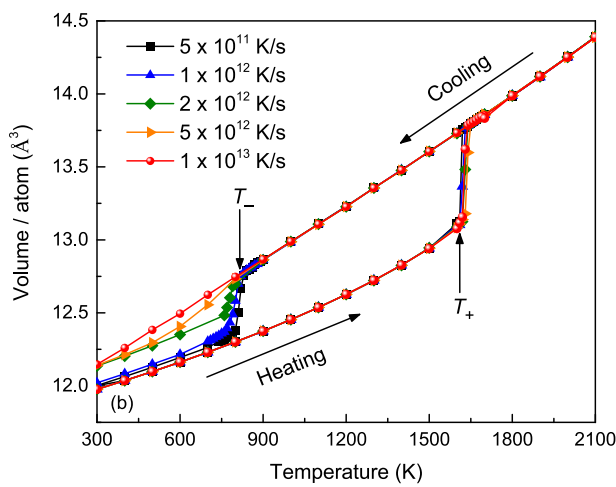
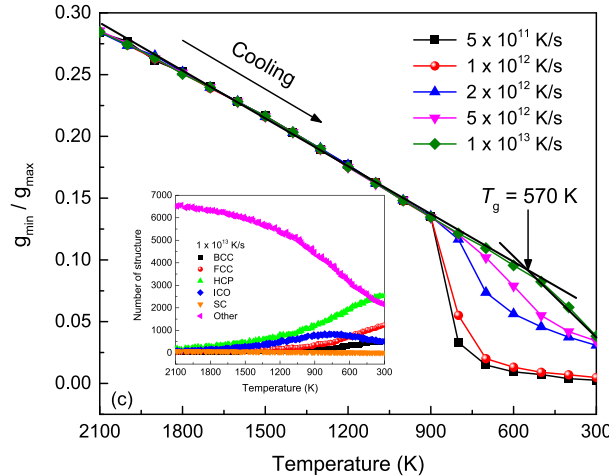
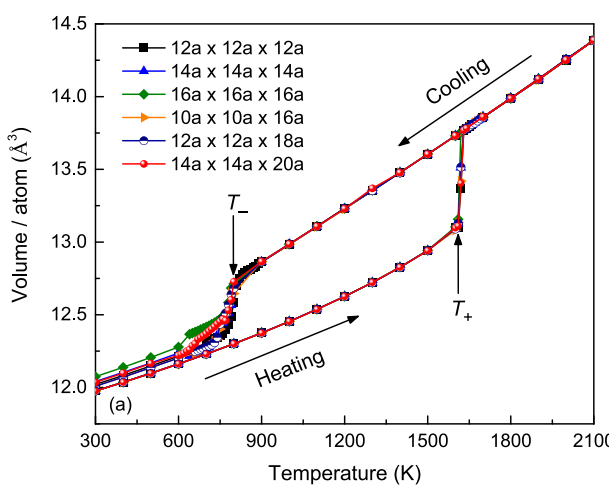


Fig. 12. Superheating and supercooling curves (a), (b), the ratio g_{\min}/g_{\max} (c), and radial distribution functions (d). (a) Atomic numbers ranging from $12a \times 12a \times 12a$ to $14a \times 14a \times 20a$. (b) Heating and cooling rates from 5×10^{11} K/s to 1×10^{13} K/s. (c) Amorphous transition temperature of the system at cooling rates from 5×10^{11} K/s to 1×10^{13} K/s, with the interpolation plotting the change in atomic structure at 1×10^{12} K/s. (d) Evolution of the radial distribution function of the system with temperature for $12a \times 12a \times 12a$ and a cooling rate of 1×10^{13} K/s, with the interpolated atomic structures corresponding to temperatures of 300, 500, 800, and 1800 K, respectively.

[120]. To further understand its nature, Fig. 12(d) illustrates the radial distribution function (RDF) curves corresponding to cooling rates from 5×10^{11} K/s to 1×10^{13} K/s and the evolution of the ratio g_{\min}/g_{\max} between the first minima g_{\min} and the first maxima g_{\max} as a function of temperature. The cooling rates from 5×10^{11} K/s to 5×10^{12} K/s exhibit a jump in g_{\min}/g_{\max} values within the temperature range of 700–900 K, as seen in Fig. 12(d). This indicates that crystallization of the system has occurred already, consistent with the trend of the supercooling curves in Fig. 12(a) and (b). Instead of a jump in the g_{\min}/g_{\max} values at a cooling rate of 1×10^{13} K/s, an amorphous structure appears [120,121]. The reason is that in the cooling process at high cooling rates, there is a relaxation period at any temperature. The relaxation process is accompanied by the disappearance of free volume, allowing the model to transition from a certain equilibrium state to a new equilibrium. Amorphous configurations are established at a certain temperature if the relaxation time of the system is so large that the relaxation process of the equilibrium state fails to keep up with its cooling processes [121]. Meanwhile, we adopt the polyhedral template matching method [122] to analyze the local structure of atoms in simple cubic (SC), body-centered cubic (BCC), hexagonal closed-packed (HCP), face-centered cubic (FCC), icosahedral (ICO), and other configurations.

The interpolation in Fig. 12(c) demonstrates that the ICO tends to increase and then decrease, exhibiting a perfect five-fold symmetric structure, which is intimately associated with the amorphous forming ability, glass transition, and mechanical behavior of the system [120]. The atomic stacking efficiency of the model decreases as the cooling rate increases and the atoms stack quite loosely in the liquid. It indicates that configurations obtained at high cooling rates have a higher degree of similarity to the liquid configurations in terms of the degree of dense stacking. Furthermore, the amorphous transition temperature T_g [123] is defined as the intersection of two straight lines with different slopes, giving a T_g of approximately 570 K, which is smaller than the available result of 673 K [124], possibly due to different interatomic potentials and the rapid cooling rate. It can be observed from the interpolation in Fig. 12(c) that the corresponding cluster of atoms remains undisturbed. The Other cluster decreases as the temperature decreases, whereas the FCC and HCP increase significantly. The RDF in the range of 300–2100 K is presented in Fig. 12(d). At a cooling rate of 1×10^{13} K/s, the first peak on the RDF curves is higher as the temperature decreases, suggesting that the greater the number of first-nearest-neighbor atoms per atom, the higher the probability of bonding of neighboring atoms within the system. The second peak of the RDF curves starts to split as the temperature drops to 700–800 K. The splitting is significant up to 500–600 K, with a high in the front and low in the back, revealing that an amorphous structure starts to form in the range of 500–600 K at a cooling rate of 1×10^{13} K/s. A weak peak emerges between the first and second peaks when the temperature drops to 400 K, demonstrating that the system starts to crystallize at 400 K. Crystallization becomes more apparent as it drops to 300 K. Despite a small amount of long-range ordered structure persisting in the system, the predominant structure is short-range ordered and disordered. This is typical of amorphous structures [120,123], as displayed in the interpolation in Fig. 12(d).

The effects of the cubic model, the cuboid model, and different heating and cooling rates on both the melting and cooling processes are presented in Table 3, where the T_m is approximately 6–9 % below the experimental temperature of 1358 K [117]. The impact of the heating rate on the melting behavior of superheated crystals is primarily achieved by causing differences in the structure of superheated crystals at the same temperature, in terms of the extent of damage to the periodic structure of the crystal. Thermodynamically, this structural difference significantly reduces the phase transition barrier of the superheated crystal. Dynamically, an increase in superheating enhances the nucleation of the liquid of the superheated crystal significantly, leading to a reduction in the melting phase transition barrier [59]. A slower cooling rate and a longer time for the crystallization process tend to result in more stable crystallization during cooling [120,121,123]. A faster

cooling rate shortens the crystallization process and inclines more toward forming a metastable state after crystallization [120,123,125]. For the cubic and cuboid models, the difference in T_m is negligible for a similar number of atoms. This also demonstrates that either a cubic or a cuboid can be applied as an initial model for the hysteresis method.

3.3. Melting temperature from Z method

To investigate the effect of the atomic number in the system on the calculation results of the Z method, the P-T curves obtained for the systems from $6a \times 6a \times 6a$ to $20a \times 20a \times 20a$ are shown in Fig. 13. An initial model of a perfect crystal is gradually heated under the NVE ensemble until it reaches the critical superheating temperature T_c . Subsequently, the system temperature automatically decreases to T_m , dividing the Z method into two stages [73], as illustrated in Fig. 14(a) and (b). In the first stage, when the system is at a temperature insufficient for the central atoms to overcome the surrounding atoms, the atoms stabilize by adjusting their positions to minimize energy. After structural relaxation has reached equilibrium at this temperature, the atoms thermally vibrate around their equilibrium position, and thus, the system appears as a solid on the P-T curves, as shown in Fig. 14(a). In the second stage, as the temperature rises above T_c , the atoms in the system gain greater ability to cross lattice barriers and escape from lattice constraints. This leads to an expansion of the atomic volume and a corresponding increase in atomic pressure with temperature. Upon melting, the temperature of the atoms drops rapidly due to heat absorption, but the pressure continues to rise as a result of the expansion of atomic volume, presenting as a liquid on the P-T curves [73], as shown in Fig. 14(b).

In addition, the atomic structure evolution relationship in Fig. 14(a) and (b) clearly reveals that the melting of the perfect crystal is a homogeneous nucleation process, distinct from crystal defects or crystal surfaces. This phenomenon is also evident in both the single method and the hysteresis method. In general, temperature promotes the melting of materials, while pressure inhibits the melting processes. The amplitude of the thermal motion of atoms in the crystal increases with temperature, facilitating the melting process. However, increased pressure imposes an additional binding force on the atoms around the equilibrium position in the crystal, thereby inhibiting the melting process [55,73]. The macroscopic manifestation is a corresponding increase in the T_m of the material, which is also consistent with the results on the P-T curves presented in Fig. 13. Comparing T_m for different systems, it is observed that the lower the number of atoms contained in the system, the higher

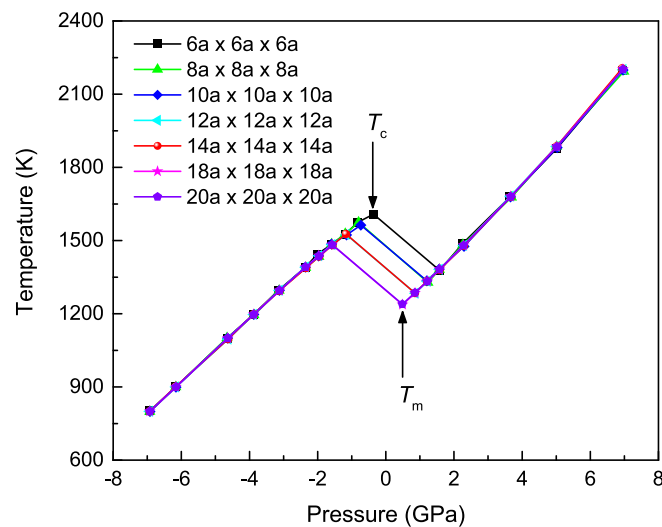


Fig. 13. Melting temperatures obtained with the Z method using systems ranging from $6a \times 6a \times 6a$ to $20a \times 20a \times 20a$, respectively.

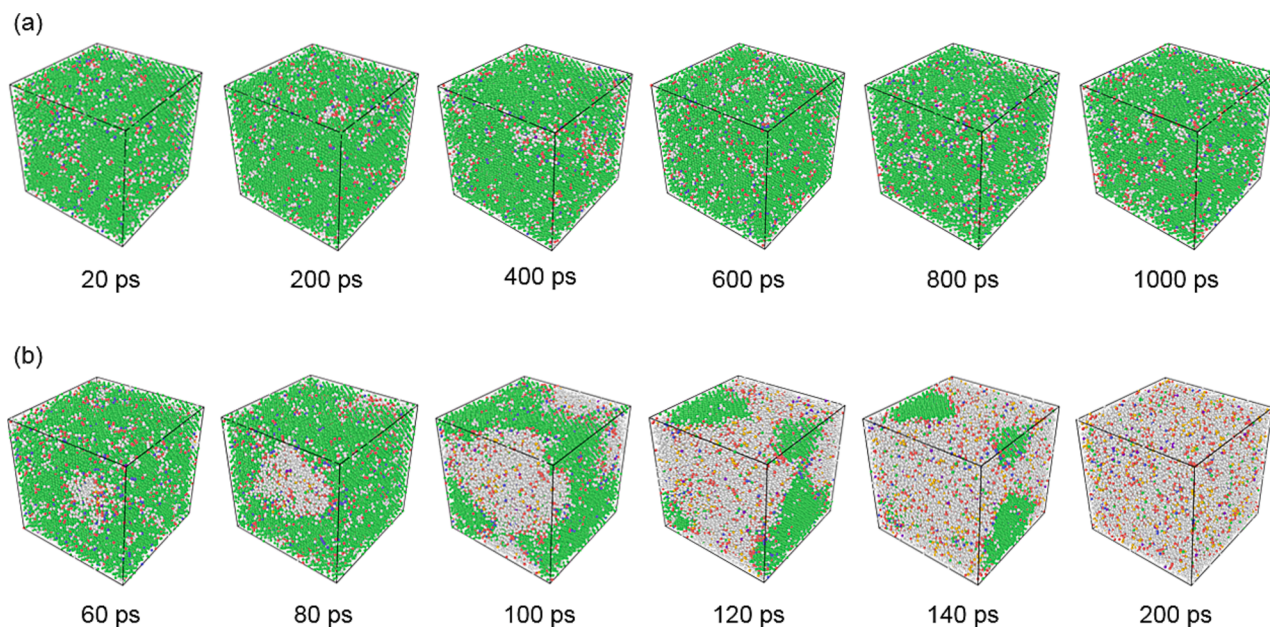


Fig. 14. A perfect crystal of $20a \times 20a \times 20a$ is gradually heated under the NVE ensemble until it reaches the critical superheating temperature. Subsequently, the system temperature automatically decreases to the melting temperature, dividing the Z method into two stages: a solid (a) at the initial temperature of 3000 K and a liquid (b) at the initial temperature of 3100 K.

both T_c and T_m . Conversely, the higher the number of atoms, the lower both T_c and T_m , as listed in Table 4, which also correlates with their corresponding pressures. In conclusion, the T_m obtained from the Z method is below the experimental value of 1358 K [117], which is a drawback of the Z method.

3.4. Melting temperature from modified Z method

Wang et al. [55] proposed a modified Z method in the system of $4a \times 4a \times 16a$ to obtain the solid–liquid coexistence state. Then, Karavaev et al. [53] supplemented the modified Z method with calculations that resulted in solid–liquid coexistence in hydrostatic equilibrium, concluding that a coexistence state could be obtained for $3a \times 3a \times 12a$. A comparative investigation is carried out using systems ranging from $3a \times 3a \times 12a$ to $4a \times 4a \times 100a$ and the simulation results are listed in **Supplementary Material**. Similar to the Z method, the modified Z method provides solid–liquid coexistence, solid, and liquid during the heating process. Thus, under the combined effect of temperature and pressure, the thermal vibrations of a localized atom in the system are enhanced enough to break free from the surrounding adjacent atoms, resulting in solid–liquid coexistence [53,55]. The NVE ensemble is applied in the Z method and modified Z method, where a small variation in atomic spacing and a significant shift in the potential energy of the system are intimately related because energy is a non-extensive quantity. This relationship is even more evident during the solid–liquid phase

transition, where a sudden change in atomic spacing results in the conversion of part of the kinetic energy into potential energy. This inevitably leads to a relatively large increase in potential energy, which is the reason for the decrease in temperature during the melting process. Furthermore, for systems of $3a \times 3a$, there is no solid–liquid coexistence as the system is smaller than $3a \times 3a \times 21a$, which is the same as for the Z method. Solid–liquid coexistence appears if the system is larger than $3a \times 3a \times 21a$ and increases as the system expands. The situation is similar for a system of $4a \times 4a$, where solid–liquid coexistence occurs with the system larger than $4a \times 4a \times 20a$. All of this implies that the number of atoms contained in the system still has a certain influence on the modified Z method. However, two unexpected states emerged during the calculation. For the system of $3a \times 3a \times 30a$, the atoms are solid at 2700 K and 2900 K, but are in solid–liquid coexistence at 2800 K, as shown in Fig. 15(a). For the system of $4a \times 4a \times 16a$, the system is solid at 3100 K, and the atoms are already in a liquid at 3200 K. There is no solid–liquid coexistence in the intermediate processes, as shown in Fig. 15(b). The results of the present work suggest that small systems ($3a \times 3a \times 12a$ and $4a \times 4a \times 16a$) fail to obtain solid–liquid coexistence for the modified Z method.

Fig. 15(c) displays the evolution of the RDFs at 2800, 3100, and 3400 K for the system of $4a \times 4a \times 100a$, along with the corresponding temperature and pressure evolution over time. All three RDFs exhibit a distinctive first peak, indicating a strongly short-range ordered structure. The intensity of the first peak of the RDF decreases slightly as the temperature continues to elevate, and subsequent peaks gradually decrease. Comparing the RDFs at 2800 K and 3400 K, it is evident that the subsequent peaks at 2800 K decrease and even smooth out. This reveals that the orderliness of the atoms weakens during the heating process, i.e., heating intensifies their thermal vibrations. The RDF at 3100 K falls between 2800 K and 3400 K. According to the relationship between temperature and pressure with time, the data at 3100 K exhibits the greatest degree of fluctuation, suggesting that the system is undergoing a solid–liquid transition [55]. During the simulation of the Z method and modified Z method [53], a volume $V = 13.20 \text{ \AA}^3$ is selected to derive T_m under ambient conditions. The effect of different volumes on the calculation of the modified Z method is also discussed, hence, volumes $V = 11.47, 11.76, 12.06, 12.45, 12.77, 13.50$, and 13.72 \AA^3 have been selected. The P - T curves for different volumes are illustrated

Table 4

Critical superheating and melting temperatures and their relative pressures obtained by the Z method using different systems, with the number of atoms of the corresponding system in parentheses.

Systems	Solid T_c (K)	Liquid T_m (K)	Solid P (GPa)	Liquid P (GPa)
$6a \times 6a \times 6a$ (864)	1608	1377	-0.3624	1.5829
$8a \times 8a \times 8a$ (2048)	1575	1328	-0.8001	1.2374
$10a \times 10a \times 10a$ (4000)	1563	1335	-0.7327	1.2039
$12a \times 12a \times 12a$ (5324)	1525	1284	-1.1654	0.8660
$14a \times 14a \times 14a$ (10976)	1527	1285	-1.1725	0.8528
$18a \times 18a \times 18a$ (23328)	1483	1237	-1.5730	0.4911
$20a \times 20a \times 20a$ (32000)	1482	1239	-1.5689	0.4852

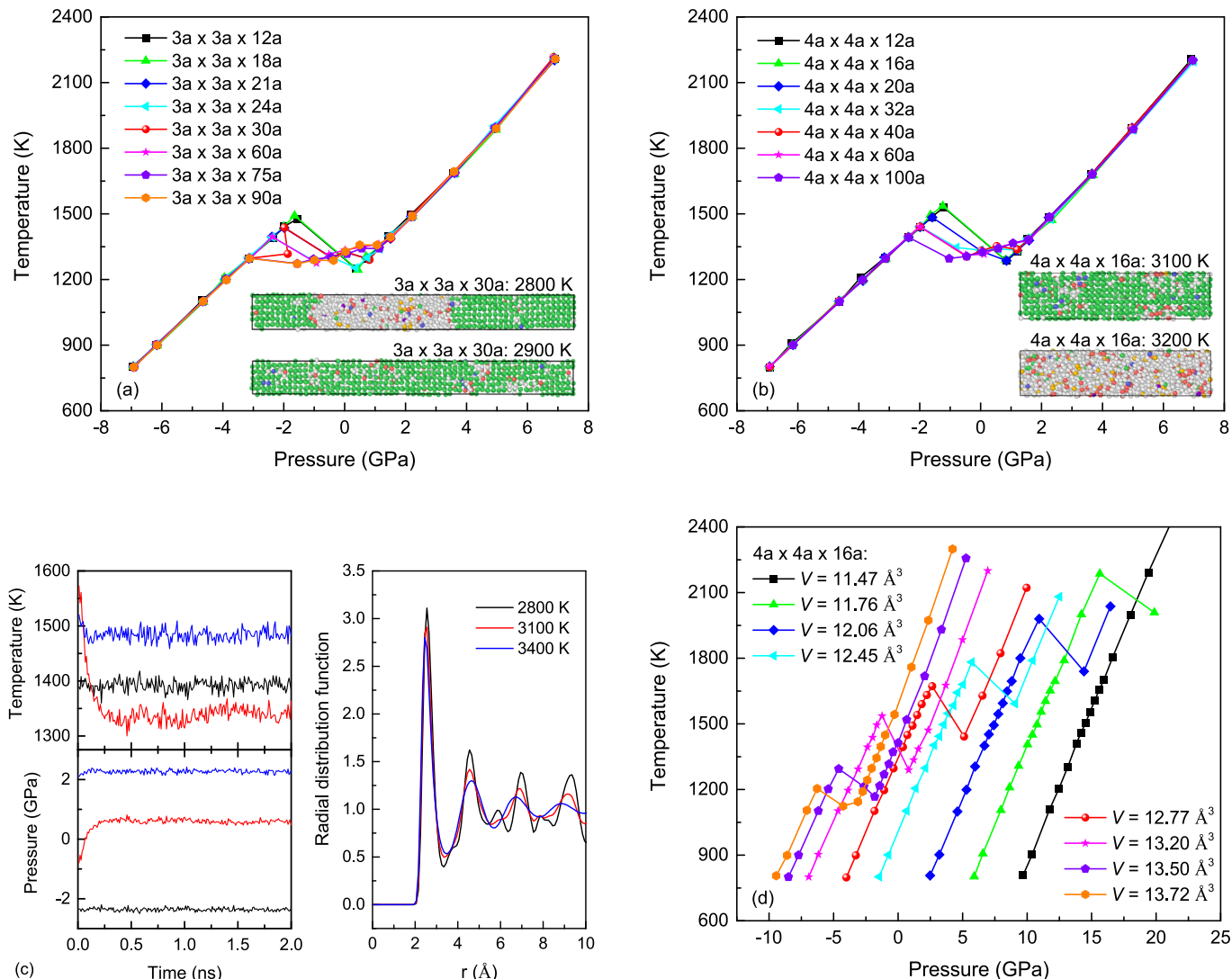


Fig. 15. In the modified Z method, (a) P - T curves for the systems from $3a \times 3a \times 12a$ to $3a \times 3a \times 90a$, (b) P - T curves for the systems from $4a \times 4a \times 12a$ to $4a \times 4a \times 100a$, (c) P - T curves for the systems from $4a \times 4a \times 100a$ at temperatures of 2800, 3100, and 3400 K, along with the corresponding RDF, and (d) P - T curves for different volumes V ranging from 11.47 \AA^3 to 13.72 \AA^3 .

in Fig. 15(d), revealing that there is no solid–liquid coexistence initially on the P - T curves as the volume increases. Solid–liquid coexistence states occur at volumes of $V = 13.50 \text{ \AA}^3$ and 13.72 \AA^3 and their corresponding pressures decrease rapidly. Combined with the calculation results of Karavaev *et al.* [53], which indicate that a change in volume has an effect on the results, that is, the initial volume influences the appearance of solid–liquid coexistence in the system.

3.5. Melting temperature from void method

To compare the effect of different defect types on the T_m within the same system, the evolution of T_m with defect size is presented in Fig. 16(a) and (b). Models I, II, III, and IV are depicted in Fig. 16(a). The cubic and sphere models are constructed with a system size of $14a \times 14a \times 14a$ (10976 atoms) and $r = 10a$ (16757 atoms), where the fractional atomic numbers of defects in Models I, II, III, and IV are 365 (3.3 %), 369 (3.4 %), 357 (3.3 %), and 321 (2.9 %), respectively. As shown in Fig. 16(a), T_m is 1340 K for both Models I and III, 1223 K for Model II, and 1434 K for Model IV. The simulations reveal that the results of Models I and III are identical, assuming similar numbers of atoms, defective atoms, and simulation conditions [116]. The calculated results for Model IV are almost 100 K higher than those for Models I and III, attributed to the

dispersed distribution of randomly deleted atoms and considerably smaller defect sizes compared to Models I and III. As a result, atoms in the vicinity of small defects are experience greater constraints from their surrounding atoms during the heating process, leading to larger superheating, as displayed in Fig. 17. This inhomogeneous nucleation process is contributed by the crystal defects. The small result for Model II is a consequence of the random arrangement of surface atoms, resulting in a higher energy. This accounts for the overall higher defect energies observed in the E - T curves compared to the other three models. The presence of defects reduces the superheating as various defects interact in a coupled form through different mechanisms, influencing the macroscopic mechanical properties of materials.

Regarding T_m , the existence of defects distorts the lattice array. Compared to perfect crystals, the internal energy is elevated, and the reduced structural stability necessitates a lower heat requirement for melting, hence a lower T_m . The impact of defect size on T_m is illustrated in Fig. 16(b) for systems of $12a \times 12a \times 12a$ (6912 atoms), $14a \times 14a \times 14a$ (10976 atoms), and $16a \times 16a \times 16a$ (16384 atoms). The increase in defect size, i.e., the increase in the surface area of the defect, weakens the chemical bonding of the atoms surrounding the defect, making them less able to resist deformation. This significantly enhances the diffusion ability of the atoms and reduces the energy barrier to nucleation in the

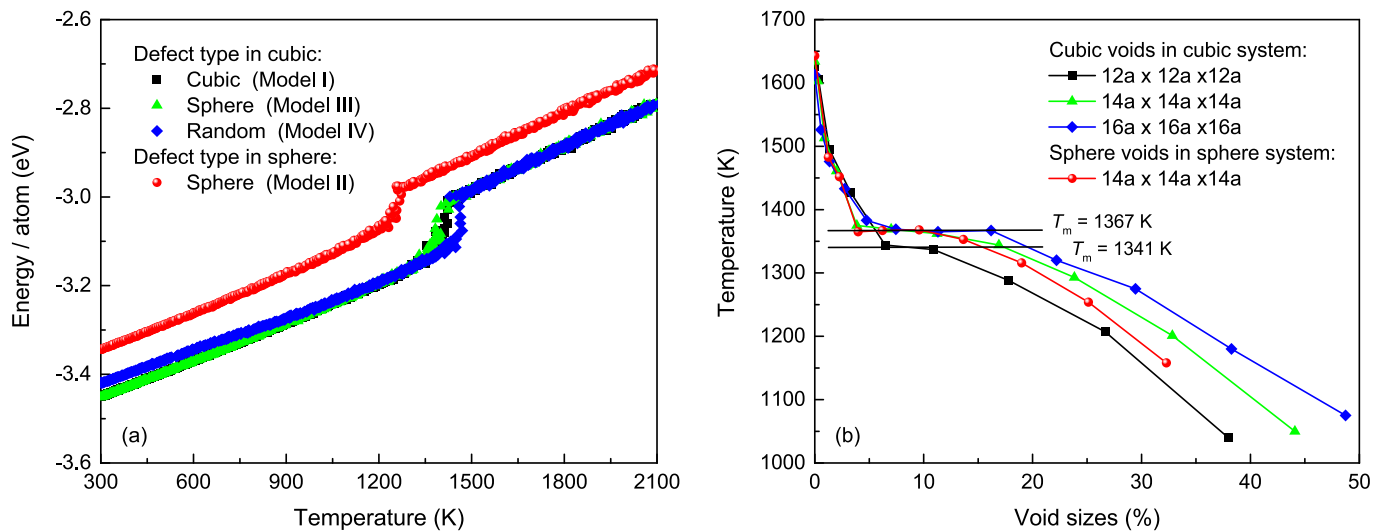


Fig. 16. Evolution of melting temperature with void defects and their dimensions, where (a) computational models of cubic defects (Model I), sphere defects (Model III), and random atomic defects (Model IV) created in the cubic model and a spherical shell model (Model II), and (b) the variation of melting temperature with the size of the four defects are presented.

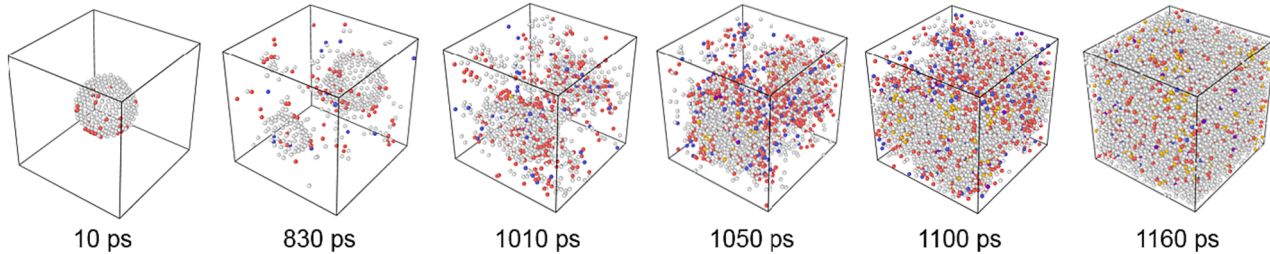


Fig. 17. Melting process for the creation of a sphere defect in the $14a \times 14a \times 14a$ system (Model III), with atomic structure evolution times of 10 ps (310 K), 830 ps (1130 K), 1010 ps (1310 K), 1050 ps (1350 K), 1100 ps (1400 K), and 1160 ps (1460 K).

liquid. For both the $14a \times 14a \times 14a$ and $16a \times 16a \times 16a$, the number of atoms fails to cause significant vibrations in the system within a 3.8 % defect concentration. A plateau is distinctly observed in the range of 3.8–16.9 % for crystal defects. At this plateau, T_m hardly varies with the increase of the defect and can be determined as an average $T_m = 1367\text{ K}$. Above 16.9 % the defect exhibits a decreasing trend in T_m , indicating that there is a specific range for accurate T_m calculation. Consequently,

defects that are too large or too small will fail to yield reliable results [12,16]. The $T_m = 1341\text{ K}$ for the $12a \times 12a \times 12a$ is below the plateau of $14a \times 14a \times 14a$ and $16a \times 16a \times 16a$, implying that for the void method, the number of atoms contained in the system also impacts the calculation results. Our research has revealed that the void method fails to effectively control the number of atoms in the defect. In response to this issue, Model III is introduced and the results are illustrated in Fig. 16

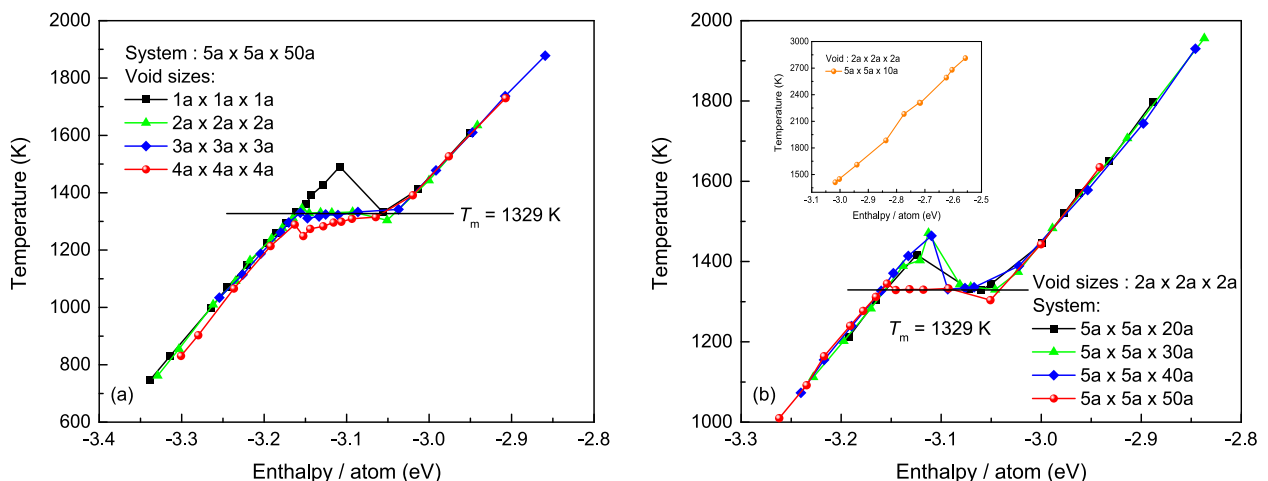


Fig. 18. Temperature versus enthalpy for (a) different defects ranging from $1a \times 1a \times 1a$ to $4a \times 4a \times 4a$ in the same system of $5a \times 5a \times 50a$, (b) the same defect size of $2a \times 2a \times 2a$ and different systems ranging from $5a \times 5a \times 10a$ to $5a \times 5a \times 50a$. The inset shows the system of $5a \times 5a \times 10a$.

(b). The $T_m = 1367$ K obtained for Model III coincides with the results of Model I, which has the advantage of better controlling the number of atoms within the defect. In fact, the T_m obtained by the void method exhibits some degree of superheating, as indicated by this analysis.

3.6. Melting temperature from modified void method

Although the void method helps reduce the superheating of the system to a certain extent by considering crystal defects, this method is not based on the solid–liquid coexistence theory. Hence, the simulations in the present study are carried out using the modified void method [59]. Fig. 18(a) and (b) depict the temperature versus enthalpy for different defects within the same system and for the same defect across different systems, respectively. To compare the effect of the atomic number contained in different defects on the simulation results, a system of $5a \times 5a \times 50a$ (5000 atoms) is selected, with defect sizes of $1a \times 1a \times 1a$ (0.3 %), $2a \times 2a \times 2a$ (1.3 %), $3a \times 3a \times 3a$ (3.4 %), and $4a \times 4a \times 4a$ (7.3 %). As depicted in Fig. 18(a), (1) solid–liquid coexistence occurs only for the enthalpy -3.06 eV corresponding to $T_m = 1332$ K for a defect of $1a \times 1a \times 1a$. (2) Solid–liquid coexistence occurs in the enthalpy region from -3.15 eV to -3.09 eV for the $2a \times 2a \times 2a$, with a temperature range from 1333 K to 1345 K. (3) Solid–liquid coexistence is observed in the enthalpy region from -3.19 eV to -3.14 eV for the $3a \times 3a \times 3a$ at 1311 – 1333 K. (4) Solid–liquid coexistence occurs in the enthalpy range from -3.15 eV to -3.09 eV for the $4a \times 4a \times 4a$ at 1249 – 1309 K. A plateau is observed in the temperature–enthalpy (T – H) curves for defects of $2a \times 2a \times 2a$ and $3a \times 3a \times 3a$ [59], corresponding to a final $T_m = 1329$ K, in good agreement with available results [59]. Although solid–liquid coexistence also occurs as the defect size increases to $4a \times 4a \times 4a$, the T – H curves at this point exhibit a sloping line, and the corresponding T_m is below the results for both the $2a \times 2a \times 2a$ and $3a \times 3a \times 3a$. The simulation results for defects demonstrate that only the defects between $2a \times 2a \times 2a$ and $3a \times 3a \times 3a$ provide a more precise T_m [59].

Furthermore, a defect of $2a \times 2a \times 2a$ is selected to further investigate the effect on systems ranging from $5a \times 5a \times 10a$ (1000 atoms) to $5a \times 5a \times 50a$, as depicted in Fig. 18(b). Among these cases: (1) atoms in the system can escape the binding of surrounding atoms as the temperature rises, and the system is already in the liquid state at $5a \times 5a \times 10a$. (2) Solid–liquid coexistence occurs at enthalpy values from -3.08 eV to -3.07 eV for the $5a \times 5a \times 20a$ (2000 atoms), and solid–liquid coexistence gradually disappears as the system evolves into the liquid. (3) Solid–liquid coexistence is observed in the enthalpy range from -3.07 eV to -3.05 eV for the $5a \times 5a \times 30a$ (3000 atoms) at 1337 – 1343 K. (4) Solid–liquid coexistence is present in the enthalpy range from -3.09 eV to -3.07 eV for the $5a \times 5a \times 40a$ (4000 atoms) at 1331 – 1336 K. Solid–liquid coexistence is observed for all four of these cases [59]. The tendency is for solid–liquid coexistence to gradually evolve into the liquid state as time increases. Observations from both the void method and modified void method reveal that, as the temperature increases for smaller numbers of atoms within the defect, atoms near the defect are still more restricted by their surrounding atoms. Only the atoms in close proximity to the defect move locally, failing to cause movement in other atoms. However, with a higher number of atoms within the defect, these atoms have a large enough distance to escape from the other atoms. This break in force equilibrium between the atoms leads to movement in other atoms within the system, reducing the overall superheating. Conversely, the system melts rapidly as the number of atoms within the defect increases. Combining the results from Fig. 18(a) and (b) for the modified void method, a more stable solid–liquid coexistence is obtained for defects of $2a \times 2a \times 2a$ and $3a \times 3a \times 3a$ in the system of $5a \times 5a \times 50a$. Compared to the void method, the results of the modified void method significantly reduce superheating.

3.7. Melting temperature from two-phase method

The impact of the proportion of solids and liquids in the two-phase approach on T_m is examined by selecting 25 %, 50 %, and 75 % of solids in the system of $10a \times 10a \times 16a$ for the initial model construction. The atomic structure of the simulation is monitored in real time to optimize computing resources. As the temperature increases, the atoms in the system gradually transition from initial solid–liquid coexistence to either a liquid or a solid. The calculation is terminated and the evolution of the system at the next temperature is calculated as time progresses. In cases where the temperature interval continually narrows without finding solid–liquid coexistence, the intermediate temperature is assumed to be the T_m of the system. Solid–liquid coexistence is certain as the temperature interval approaches 0.1 K, or even 0.01 K. With a 25 % solid state as the initial model, the atomic number density is displayed in Fig. 19. The whole system remains in a solid state at a temperature of 1324 K because the temperature is below T_m , reducing the vibration amplitude of the atoms. At 1330 K, the system melts completely as the temperature exceeds T_m . At 1326 K, the system is in solid–liquid coexistence, indicating that the temperature at this stage can be assumed to be T_m . The T_m obtained for the solid simulations at 50 % and 75 % are 1328 K and 1329 K respectively, indicating that the proportion of solids and liquids has no significant effect on the final T_m [67]. The effect of the number of atoms in the two-phase method on the results is also discussed for simulations ranging from $5a \times 5a \times 10a$ to $20a \times 20a \times 32a$, and the summarized T_m is presented in Table 5. The initial system of $5a \times 5a \times 10a$ for the two-phase method yields a $T_m = 1375$ K, significantly higher than the results for other systems. This study suggests that an accurate $T_m = 1324$ K can be achieved for Cu atoms with a minimum two-phase simulation size of $6a \times 6a \times 12a$. The $T_m = 1327$ K obtained for a system of $20a \times 20a \times 32a$ indicates that the number of atoms within a certain range has a weak impact on the simulation results. Meanwhile, Zou et al. [59] obtained a T_m of 1316 ± 3 K for Cu using the thermodynamic integral method, closely aligning with the results obtained in this work using the two-phase approach.

3.8. Melting temperature from sandwich method

The effect of one, two, four, and six solid–liquid interfaces on the melting process is discussed in the sandwich approach [67]. In order to eliminate the influence of pure solids and pure liquids on the solid–liquid interface under periodic boundary conditions, the

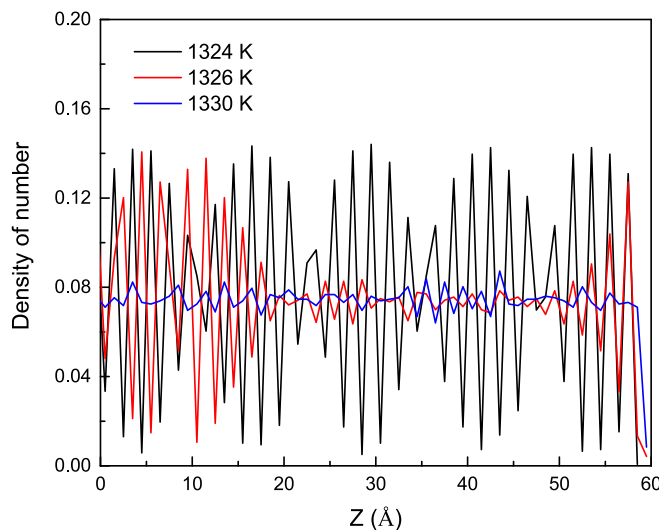


Fig. 19. Evolution of the number density in the melting process at (a) 1324 , (b) 1326 , and (c) 1330 K for the system of $10a \times 10a \times 16a$ in the two-phase method.

Table 5

The effect on the melting temperature is evaluated for a system with atomic numbers ranging from $5a \times 5a \times 10a$ to $20a \times 20a \times 32a$ in the initial model simulated using the two-phase method with 50 % solids. The effect on the melting temperature is also evaluated for a system of $10a \times 10a \times 16a$ with 25 %, 50 %, and 75 % solids, with the number of atoms in the corresponding system in parentheses.

Systems	Solid (%)	T_m (K)
$5a \times 5a \times 10a$ (1000)	50	1375 ± 5
$6a \times 6a \times 12a$ (1728)	50	1324 ± 1
$8a \times 8a \times 16a$ (4096)	50	1326 ± 1
$10a \times 10a \times 16a$ (6400)	25	1326 ± 1
	50	1325 ± 2
	75	1329 ± 1
$12a \times 12a \times 18a$ (10368)	50	1328 ± 1
$12a \times 12a \times 20a$ (11520)	50	1328 ± 1
$12a \times 12a \times 30a$ (17280)	50	1327 ± 1
$12a \times 12a \times 42a$ (24192)	50	1325 ± 1
$15a \times 15a \times 24a$ (21600)	50	1327 ± 1
$20a \times 20a \times 32a$ (51200)	50	1327 ± 1

inter-interface spacing should be large enough and the solid–liquid interface spacing is assumed to be 6 Å. In the system of $12a \times 12a \times 30a$, the evolution of the solid–liquid interface with time during the melting process at (a) 1321, (b) 1324, and (c) 1330 K is presented in Fig. 20, respectively. The initial solid–liquid interface configuration is the same for all three temperatures. At 1321 K, the two liquid regions gradually engulf the middlemost solid region with increasing time, as shown in Fig. 20, and thus the solid and liquid atoms partly occupy each other. At 800 ps, the system has evolved into a solid, indicating that 1321 K is below T_m , and conversely, 1330 K is above T_m . Therefore, the temperature interval is reduced until 1323, 1324, and 1325 K, and the solid–liquid interface appears in the system. The solid–liquid interface is stable with time, and 1324 K is adopted as the T_m of the system. In addition, the differences between one, two, four, and six solid–liquid interfaces are discussed separately and the results are listed in Table 6. Melting typically occurs at the solid–liquid interface and at defects, both of which are significant factors in reducing T_m . A distinction is observed in the results for two, four, and six solid–liquid interfaces in the

Table 6

Discusses the effect of one, two, four, and six solid–liquid interfaces on the melting temperature for simulated systems of $12a \times 12a \times 18a$, $12a \times 12a \times 30a$, and $12a \times 12a \times 42a$, with the number of atoms of the corresponding system in parentheses.

Systems	Solid (liquid) spacing (Å)	Solid–liquid interfaces	T_m (K)
$12a \times 12a \times 18a$ (10368)	6	1	1328 ± 1
	6	2	1326 ± 1
$12a \times 12a \times 30a$ (17280)	6	1	1327 ± 1
	6	4	1324 ± 1
$12a \times 12a \times 42a$ (24192)	6	1	1325 ± 1
	6	6	1322 ± 1

sandwich method compared to one interface, i.e., the higher the number of solid–liquid interfaces, the lower the T_m . However, it should be noted that the T_m obtained in this work using the EAM potentials is below the experimental value [117]. This suggests that the more interfaces there are, the further the obtained T_m is from the experimental value, a phenomenon commonly observed in other researches [55,59,126]. In addition, solid–liquid interface energy is an essential parameter influencing the melting and crystallization processes. The existence of solid–liquid interface energy causes inconsistencies in the superheating and supercooling of the material during melting and crystallization.

We also calculated the solid–liquid interface energy for the system of $12a \times 12a \times 30a$, formulated as $\gamma_{SL} = \Gamma \cdot \Delta S$, where Γ is the Gibbs–Thomson coefficient, and the experimental result is 1.29×10^{-7} K·m [127]. ΔS is the entropy of melting and is calculated as $\Delta S = \frac{\rho_s \cdot \Delta H}{T_m}$, where ρ_s is the number density of the solid phase, 8.467×10^{28} atom/m³, and ΔH is the latent heat of melting, 2.065×10^{-20} J/atom, and T_m is the melting temperature of the corresponding system, taken to be 1327 K. Finally, the obtained $\gamma_{SL} = 0.170$ J/m²,

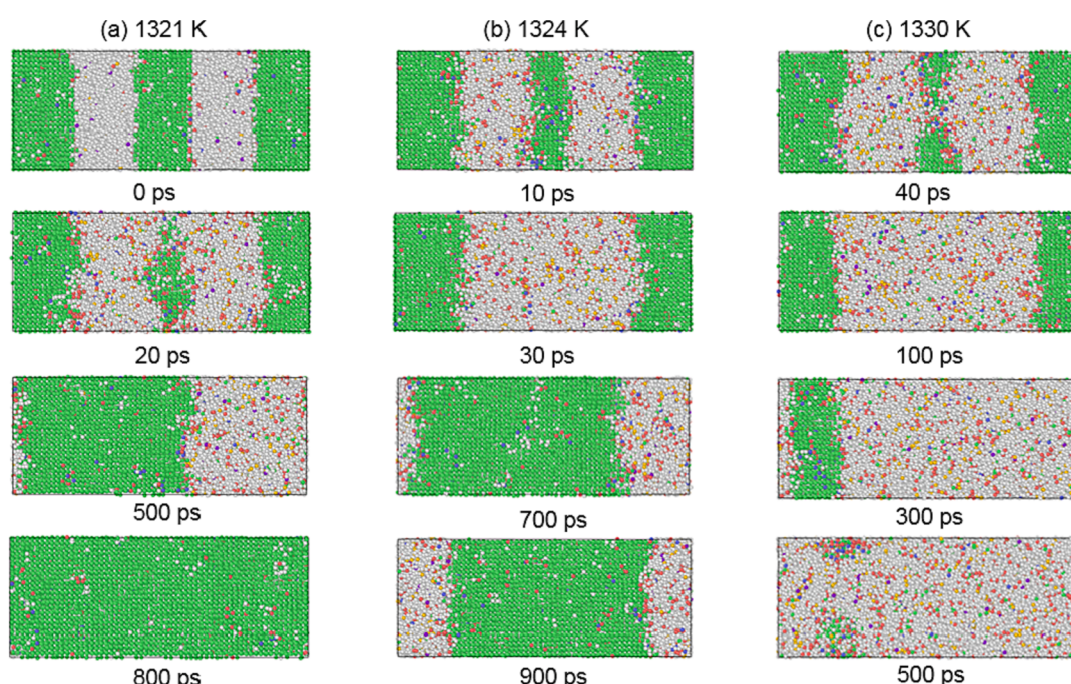


Fig. 20. Evolution of the solid–liquid interface with time during the melting process at (a) 1321, (b) 1324, and (c) 1330 K for the system of $12a \times 12a \times 30a$ using the sandwich method.

which agrees well with the experimental results of $\gamma_{SL}^{Exp.} = 0.198 \text{ J/m}^2$ [128], indicates that the adopted EAM potentials will underestimate the T_m of Cu, significantly below the experimental value of 1358 K [117], and, similarly, will also underestimate γ_{SL} .

3.9. Melting temperature from modified two-phase method

Based on the analysis above, the results of the void method and the modified void method research reveal differences in calculations for cubic defects, sphere defects, and random atomic defects. Among these, the cubic defects and sphere defects yielded better results than random atomic defects. Therefore, in this part of the work only the cubic defects are considered for investigation. To discuss the effect of the number of defect atoms on T_m during simulations of the modified two-phase method, a $12a \times 12a \times 30a$ system is adopted, with defects ranging from $2a \times 2a \times 2a$ to $7a \times 7a \times 7a$. From Table 7 it can be seen that the defect size is $0a \times 0a \times 0a$, i.e., the two-phase method, which corresponds to a $T_m = 1327 \text{ K}$. The T_m values are 1330, 1326, 1325, 1312, and 1294 K in the order of defects from $2a \times 2a \times 2a$ to $6a \times 6a \times 6a$. Compared to the two-phase approach, the movement of defects during the heating process increases the total energy of the system, leading to pre-melting. The most notable phenomenon is the decrease in the material's T_m due to the reduced energy difference between the solid and liquid phases required for melting. The T_m tends to decrease with increasing defect size, exceeding $6a \times 6a \times 6a$ (8%). The calculations reveal an unreasonable result for the system of $12a \times 12a \times 30a$ as the defects exceed $7a \times 7a \times 7a$ (9%). The increased surface area of the defect makes the atomic bonds around the defect less able to resist deformation, resulting in a T_m below the actual value. We also analyzed the minimum system for the modified two-phase method, with the T_m values of 1326 K and 1322 K for the systems of $8a \times 8a \times 16a$ and $6a \times 6a \times 12a$, respectively. It is revealed that $6a \times 6a \times 12a$ can be applied as the initial system for the modified two-phase method, consistent with the minimum system for the two-phase method.

Furthermore, when comparing the T_m calculated by the two-phase method and the modified two-phase method, it is challenging to judge the advantage because the EAM potentials underestimate the T_m of Cu atoms [55,59,126]. Hence, MgO and ZnO are selected for comparative analysis with experimental T_m values of 3080 K [129] and 2242 K [130], using the Buckingham and Morse potentials [131,132] and the system of $8a \times 8a \times 16a$, with the same parameters as before. The two-phase

Table 7

The impact of the number of atoms within different defects on their melting temperatures is discussed for the Cu, MgO, and ZnO during the calculation of the modified two-phase method, where the defect size of $0a \times 0a \times 0a$ equals the traditional two-phase method.

Systems	Void sizes	T_m (K)
Cu		
$12a \times 12a \times 30a$ (17280)	$0a \times 0a \times 0a$	1327 ± 1
	$2a \times 2a \times 2a$	1330 ± 1
	$3a \times 3a \times 3a$	1326 ± 1
	$4a \times 4a \times 4a$	1325 ± 2
	$5a \times 5a \times 5a$	1312 ± 3
	$6a \times 6a \times 6a$	1294 ± 3
	$7a \times 7a \times 7a$	1255 ± 5
$8a \times 8a \times 16a$ (4096)	$2a \times 2a \times 2a$	1326 ± 1
$6a \times 6a \times 12a$ (1728)	$2a \times 2a \times 2a$	1322 ± 1
MgO		
$8a \times 8a \times 16a$ (8092)	$0a \times 0a \times 0a$	3305 ± 3
	$2a \times 2a \times 2a$	3295 ± 5
	$3a \times 3a \times 3a$	3285 ± 5
	$3.5a \times 3.5a \times 3.5a$	3280 ± 5
ZnO		
$8a \times 8a \times 16a$ (6144)	$0a \times 0a \times 0a$	2300 ± 5
	$2a \times 2a \times 2a$	2285 ± 5
	$3a \times 3a \times 3a$	2270 ± 5
	$3.5a \times 3.5a \times 3.5a$	2265 ± 5

method gives $T_m = 3305 \text{ K}$ for MgO and the modified two-phase method gives T_m values of 3295, 3285, and 3280 K at defects of $2a \times 2a \times 2a$ (1%), $3a \times 3a \times 3a$ (3.8%), and $3.5a \times 3.5a \times 3.5a$ (8.4%), respectively. It can be noticed that the modified two-phase method improves the T_m by almost 25 K compared to the two-phase method, especially for materials where the calculated model overestimates the T_m . The T_m obtained by the traditional two-phase method for ZnO is 2300 K. However, the T_m obtained by the modified two-phase method with defects of $2a \times 2a \times 2a$ (1.4%), $3a \times 3a \times 3a$ (5.2%), and $3.5a \times 3.5a \times 3.5a$ (10%) are, in order, 2285 K, 2270 K, and 2265 K. Moreover, the superheating of T_m is lower compared to the traditional two-phase method and the one obtained by Wang et al [132]. Finally, the results for Cu, MgO, and ZnO exhibit a significant deviation for defects exceeding $4a \times 4a \times 4a$ (10%). For the modified two-phase method, a reasonable T_m can be achieved by combining the calculations for Cu, MgO, and ZnO with defects below 10%.

3.10. Comparison of melting methods

Fig. 21 presents the comparative results calculated by the melting methods adopted in this study, including simulation accuracy, efficiency, and individual features. During the simulation of the single-phase method, a reasonable $T_m = 1649 \pm 10 \text{ K}$ is obtained for a simulated system of $8a \times 8a \times 8a$. The difference in T_m between a heating rate of $1 \times 10^{11} \text{ K/s}$ and $1 \times 10^{12} \text{ K/s}$ is narrow, but the computational time for a heating rate of $1 \times 10^{11} \text{ K/s}$ is doubled. Although the single-phase approach has a disadvantage in calculating the T_m values, it can be utilized to discuss the superionic behavior of materials that does not involve superheating [60,71,133,134]. Meanwhile, the difference in T_m obtained from the cubic and cuboid models is insignificant, i.e., they can both be considered as initial models for the single-phase approach. The results obtained by adding the vacuum layer model decrease T_m due to the presence of surface atoms. However, the stability of the atomic structure in the sphere model is less stable than in the cubic and cuboid models. In this work, the superheating of T_m is in the range of 18–27 % for the single-phase approach. During the simulation of the hysteresis method, the cubic and cuboid models are selected as the simulated systems, and the T_m difference is slightly different in the case of a similar number of atoms. The T_m obtained from the simulation is about 6–9 % below the experimental values [117]. In addition, the heating rate exceeds $1 \times 10^{14} \text{ K/s}$, leading to the limiting temperature of crystal superheating. The system will evolve to an amorphous state with cooling rates higher than $1 \times 10^{13} \text{ K/s}$. Simultaneously, both heating and cooling processes need to be calculated, and their computation is considerable. For both the Z method and the modified Z method, the T_m obtained by the Z method is obviously underestimated and fails to control the pressure. However, the modified Z method, based on solid-liquid coexistence, provides a remarkable improvement in the accuracy of T_m . The results indicate that solid-liquid coexistence occurs in the simulated systems of $3a \times 3a \times 21a$ and $4a \times 4a \times 20a$ for the modified Z method. Additionally, both the Z method and the modified Z method are highly demanding in terms of computer performance, with typical simulation times of 2 ns at each temperature, and the analysis of the simulation times is provided in the **Supplementary Material**.

For the void method and the modified void method, the issue of superheating during melting caused by the single-phase method is substantially reduced due to the existence of crystal defects. Compared to the single-phase method, the hysteresis method, and the Z method, the void method gives results closer to the experimental values in the defect range of 3.8–16.9 %. However, the void method is not based on solid-liquid coexistence. Instead, the modified void method achieves solid-liquid coexistence by replacing the cubic model with a cuboid model, resulting in a more reliable T_m obtained for a defect range of 0.3–7.3 %. Moreover, it also has a simulation time of 2 ns at each temperature. In the two-phase approach, the differences in T_m obtained for the 25%, 50%, and 75% solid percentage simulations are negligible,

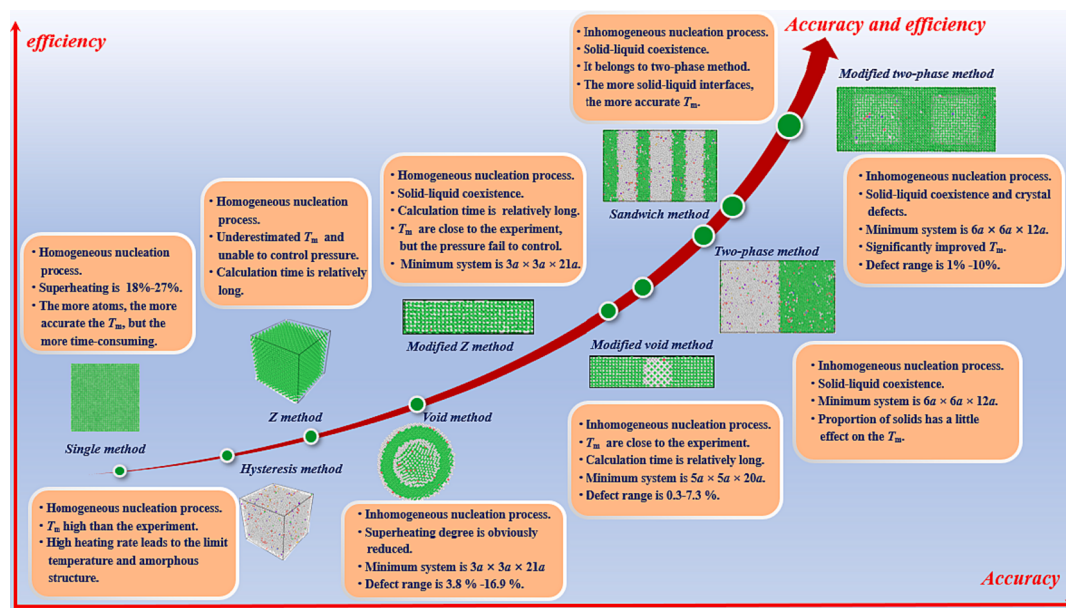


Fig. 21. A comprehensive comparison of the accuracy and efficiency of single-phase method, hysteresis method, Z method, modified Z method, void method, modified void method, two-phase method, sandwich method, and modified two-phase method is investigated using molecular dynamics simulations.

implying that the percentage of solids and liquids in the simulated system has little effect on the final results. A reasonable $T_m = 1322 \pm 1$ K is obtained for the two-phase method when the smallest simulation dimension is $6a \times 6a \times 12a$. The findings of the sandwich method with two, four, and six solid-liquid interfaces versus one imply that the higher the number of solid-liquid interfaces, the closer the T_m obtained is to the experiment. For the modified two-phase approach, a simulation dimension of $6a \times 6a \times 12a$ provides an accurate T_m , which is consistent with the minimal simulation system of the traditional two-phase approach. The modified two-phase method provides nearly 25 K and 35 K higher T_m for MgO and ZnO than the traditional two-phase method in the present work.

4. Conclusions

A comprehensive comparison of the accuracy and efficiency of the single-phase method, hysteresis method, Z method, modified Z method, void method, modified void method, two-phase method, sandwich method, and modified two-phase method is investigated. We propose a modified two-phase method to obtain a T_m improvement of almost 35 K compared to the results of the two-phase method, while also requiring lower computational due to the removal of atoms by the crystal defects. The sandwich method provides superior results to the two-phase method in terms of the accuracy of simulation results, attributed to the presence of more solid-liquid interfaces, although computational effort is comparable. While the modified Z method, derived from solid-liquid coexistence theory, is frequently applied in AIMD, its computational volume remains a challenge. In comparison, the modified void method enables control of the pressure in the system and allows a similar T_m to be obtained with the two-phase method for a range of crystal defects. For the single-phase method, hysteresis method, Z method, and void method, the calculations are complicated, and the results are less accurate than those from solid-liquid coexistence methods. Particularly, the machine learning method is adopted to develop high-precision potential models, overcoming the limitations of traditional potentials, including low accuracy and poor portability. This approach allows for independence from empirical parameters and has the potential to enhance the efficiency and accuracy of T_m calculations, making calculation methods based on solid-liquid coexistence theory increasingly effective.

CRediT authorship contribution statement

Xinwei Wang: Methodology, Investigation, Formal analysis, Writing – original draft. **Mengxin Yang:** Formal analysis, Methodology. **Xiaolian Gai:** Methodology. **Yibo Sun:** Formal analysis, Data curation. **Bohan Cao:** Formal analysis. **Jiajin Chen:** Methodology. **Min Liang:** Investigation. **Fubo Tian:** Resources. **Liang Li:** Formal analysis.

Declaration of competing interest

The authors declare that they have no known competing financial interests or personal relationships that could have appeared to influence the work reported in this paper.

Data availability

No data was used for the research described in the article.

Acknowledgements

This work was supported by the National Natural Science Foundation of China (Nos. 11574109, 91745203), and parts of calculations were performed in the High-Performance Computing Center (HPCC) of Jilin University.

Appendix A. Supplementary data

Supplementary data to this article can be found online at <https://doi.org/10.1016/j.molliq.2023.123924>.

References

- [1] M. Schörner, B.B.L. Witte, A.D. Baczewski, A. Cangi, R. Redmer, *Ab initio* study of shock-compressed copper, *Phys. Rev. B* 106 (2022) 054304.
- [2] F. Saiz, Molybdenum disulfide under extreme conditions: An *ab initio* study on its melting, *J. Appl. Phys.* 133 (2023) 105102.
- [3] C. Cui, J. Xian, H. Liu, F. Tian, X. Gao, H. Song, Melting curve of magnesium up to 460 GPa from *ab initio* molecular dynamics simulations, *J. Appl. Phys.* 131 (2022) 195901.
- [4] Z.L. Liu, X.L. Zhang, L.C. Cai, Shock melting method to determine melting curve by molecular dynamics: Cu, Pd, and Al, *J. Chem. Phys.* 143 (2015) 114101.
- [5] M.N. Magomedov, Study of the melting temperature baric dependence for Au, Pt, Nb, *Vacuum* 213 (2023) 112079.

- [6] G. Weck, V. Recoules, J.A. Queyroux, F. Datchi, J. Bouchet, S. Ninet, G. Garbarino, M. Mezouar, P. Loubeyre, Determination of the melting curve of gold up to 110 GPa, *Phys. Rev. B* 101 (2020) 014106.
- [7] J. Whaley-Baldwin, Structures of elemental potassium at terapascal pressures, *Phys. Rev. B* 107 (2023) 024106.
- [8] Z.M. Geballe, N. Holtgrewe, A. Karandikar, E. Greenberg, V.B. Prakapenka, A. F. Goncharov, Latent heat method to detect melting and freezing of metals at megabar pressures, *Phys. Rev. Mater.* 5 (2021) 033803.
- [9] D. Errandonea, High-pressure melting curves of the transition metals Cu, Ni, Pd, and Pt, *Phys. Rev. B* 87 (2013) 054108.
- [10] H.K. Hieu, Melting of solids under high pressure, *Vacuum* 109 (2014) 184–186.
- [11] X. Fan, X. Chen, D. Pan, Y. Liu, P. Liu, M. Li, Localization and delocationization of surface disordering in surface mediated melting, *Phys. Rev. B* 104 (2021) 134204.
- [12] X.-W. Wang, X.-W. Sun, T. Song, J.-H. Tian, Z.-J. Liu, Prediction of the melting curve and phase diagram for CaO using newly developed interatomic potentials, *Vacuum* 209 (2023) 111717.
- [13] T.D. Cuong, N.Q. Hoc, N.D. Trung, N.T. Thao, A.D. Phan, Theoretical predictions of melting behaviors of hcp iron up to 4000 GPa, *Phys. Rev. B* 106 (2022) 094103.
- [14] P. Parisiades, F. Cova, G. Garbarino, Melting curve of elemental zirconium, *Phys. Rev. B* 100 (2019) 054102.
- [15] P. Vyas, A.B. Patel, N.K. Bhatt, First-principles study of thermoelasticity and structural phase diagram of CaO, *Phys. Rev. B* 107 (2023) 014107.
- [16] C.M. Alvares, G. Deffrennes, A. Pisch, N. Jakse, Thermodynamics and structural properties of CaO: A molecular dynamics simulation study, *J. Chem. Phys.* 152 (2020) 084503.
- [17] T. Bgasheva, T. Falyakhov, S. Petukhov, M. Sheindlin, A. Vasin, P. Vervikishko, Laser-pulse melting of calcium oxide and some peculiarities of its high-temperature behavior, *J. Am. Ceram. Soc.* 104 (2021) 3461–3477.
- [18] G. Zhang, X. Fan, Q. Zhang, Q. Li, Y. Wu, M. Li, Partial disordering and homogeneous melting in multicomponent systems, *Acta Mater.* 239 (2022) 118281.
- [19] Y. Zhang, Y. Tan, H.Y. Geng, N.P. Salke, Z. Gao, J. Li, T. Sekine, Q. Wang, E. Greenberg, V.B. Prakapenka, J.-F. Lin, Melting curve of vanadium up to 256 GPa: Consistency between experiments and theory, *Phys. Rev. B* 102 (2020) 214104.
- [20] X. Fan, D. Pan, M. Li, Rethinking Lindemann criterion: A molecular dynamics simulation of surface mediated melting, *Acta Mater.* 193 (2020) 280–290.
- [21] C. Niu, H. Zhang, J. Zhang, Z. Zeng, X. Wang, Ultralow Melting Temperature of High-Pressure Face-Centered Cubic Superionic Ice, *J. Phys. Chem. Lett.* 13 (2022) 7448–7453.
- [22] A. Dewaele, P. Loubeyre, F. Occelli, O. Marie, M. Mezouar, Toroidal diamond anvil cell for detailed measurements under extreme static pressures, *Nat. Commun.* 9 (2018) 2913.
- [23] N. Dubrovinskaia, L. Dubrovinsky, N.A. Solopova, A. Abakumov, S. Turner, M. Hanfland, E. Bykova, M. Bykov, C. Prescher, V.B. Prakapenka, Terapascal static pressure generation with ultrahigh yield strength nanodiamond, *Sci. Adv.* 2 (2016) e1600341.
- [24] P. Parisiades, A review of the melting curves of transition metals at high pressures using static compression techniques, *Crystals* 11 (2021) 416.
- [25] P. Kalita, J. Brown, P. Specht, S. Root, M. White, J.S. Smith, Dynamic x-ray diffraction and nanosecond quantification of kinetics of formation of β -zirconium under shock compression, *Phys. Rev. B* 102 (2020) 060101.
- [26] J.H. Egger, D.G. Hicks, P.M. Celliers, D.K. Bradley, R.S. McWilliams, R. Jeanloz, J.E. Miller, T.R. Boehly, G.W. Collins, Melting temperature of diamond at ultrahigh pressure, *Nat. Phys.* 6 (2009) 40–43.
- [27] T.S. Duffy, R.F. Smith, Ultra-High Pressure Dynamic Compression of Geological Materials, *Front. Earth Sci.* 7 (2019) 23.
- [28] J.H. Nguyen, N.C. Holmes, Melting of iron at the physical conditions of the Earth's core, *Nature* 427 (2004) 339–342.
- [29] J.R. Morris, C.Z. Wang, K.M. Ho, C.T. Chan, Melting line of aluminum from simulations of coexisting phases, *Phys. Rev. B* 49 (1994) 3109.
- [30] T. Ninomiya, Theory of Melting, Dislocation Model. I, *J. Phys. Soc. Jpn.* 44 (1978) 263–268.
- [31] M. Born, Thermodynamics of Crystals and Melting, *J. Chem. Phys.* 7 (1939) 591–603.
- [32] V.V. Kechin, Melting curve equations at high pressure, *Phys. Rev. B* 65 (2001) 052102.
- [33] S.S. Kushwah, Y.S. Tomar, A.K. Upadhyay, On the volume-dependence of the Grüneisen parameter and the Lindemann law of melting, *J. Phys. Chem. Solids* 74 (2013) 1143–1145.
- [34] F. Simon, G. Glatzel, Bemerkungen zur schmelzdruckkurve, *Z. Anorg. Allg. Chem.* 178 (1929) 309.
- [35] E.A. Kraut, G.C. Kennedy, New melting law at high pressures, *Phys. Rev.* 151 (1966) 668.
- [36] Z. Wang, The melting of Al-bearing perovskite at the core-mantle boundary, *Phys. Earth Planet. in.* 115 (1999) 219.
- [37] Z. Wang, P. Lazor, S. Saxena, A simple model for assessing the high pressure melting of metals: nickel, aluminum and platinum, *Physica B* 293 (2001) 408–416.
- [38] J. Jiang, X. Zhang, F. Ma, S. Dong, W. Yang, M. Wu, Molecular dynamics simulation of the crystal structure evolution of titanium under different Tdamp values and heating/cooling rates, *Chem. Phys. Lett.* 763 (2021) 138187.
- [39] R.W. Cahn, Materials science: melting and the surface, *Nature* 323 (1986) 668–669.
- [40] C. Wen, D. Yun, X. He, Y. Xin, W. Li, Z. Sun, Applying multi-scale simulations to materials research of nuclear fuels: A review, *Mater. Rep. Energy* 1 (2021) 100048.
- [41] J. Han, Y. Chen, J. Wang, G. Zhang, H. Wang, A review of molecular dynamics simulation in studying surface generation mechanism in ultra-precision cutting, *Int. J. Adv. Manuf. Tech.* 122 (2022) 1195–1231.
- [42] A. Kedharnath, R. Kapoor, A. Sarkar, Classical molecular dynamics simulations of the deformation of metals under uniaxial monotonic loading: A review, *Comput. Struct.* 254 (2021) 106614.
- [43] N. Van Nghia, N.D. Chinh, H.K. Hieu, Theoretical prediction of melting curves of gold and silver up to pressure 150 GPa, *Vacuum* 202 (2022) 111189.
- [44] T. Zhang, S. Wang, H. Song, S. Duan, H. Liu, Melting curve of vanadium up to 470 GPa simulated by ab initio molecular dynamics, *J. Appl. Phys.* 126 (2019) 205901.
- [45] W.-J. Zhang, Y.-F. Peng, Z.-L. Liu, Molecular dynamics study of melting curve, entropy of fusion and solid-liquid interfacial energy of cobalt under pressure, *Physica B* 440 (2014) 33–40.
- [46] F. Delogu, Structural and energetic properties of unsupported Cu nanoparticles from room temperature to the melting point: molecular dynamics simulations, *Phys. Rev. B* 72 (2005) 205418.
- [47] G. Chen, C. Wang, P. Zhang, The non-equilibrium crystallization of Cu₃Au with cooling rate near criticality, *Comput. Mater. Sci.* 112 (2016) 80–86.
- [48] W.-J. Zhang, Z.-L. Liu, Y.-F. Peng, Molecular dynamics simulations of the melting curves and nucleation of nickel under pressure, *Physica B* 449 (2014) 144–149.
- [49] S.N. Luo, A. Strachan, D.C. Swift, Nonequilibrium melting and crystallization of a model Lennard-Jones system, *J. Chem. Phys.* 120 (2004) 11640–11649.
- [50] C. Loyola, S. Davis, J. Peralta, Nonequilibrium, highly inhomogeneous melting in the microcanonical ensemble, *Physica A* 595 (2022) 127045.
- [51] A.B. Belonoshko, N. Skorodumova, A. Rosengren, B. Johansson, Melting and critical superheating, *Phys. Rev. B* 73 (2006) 012201.
- [52] I.A. Kruglov, A. Yanilkin, A.R. Organov, P. Korotaev, Phase diagram of uranium from *ab initio* calculations and machine learning, *Phys. Rev. B* 100 (2019) 174104.
- [53] A.V. Karavaev, V.V. Dremov, T.A. Pravishkina, Precise calculation of melting curves by molecular dynamics, *Comput. Mater. Sci.* 124 (2016) 335–343.
- [54] C.M. Liu, C. Xu, Y. Cheng, X.R. Chen, L.C. Cai, Melting curves and structural properties of tantalum from the modified-Z method, *J. Appl. Phys.* 118 (2015) 235901.
- [55] S. Wang, G. Zhang, H. Liu, H. Song, Modified Z method to calculate melting curve by molecular dynamics, *J. Chem. Phys.* 138 (2013) 134101.
- [56] S. Wang, H. Liu, G. Zhang, H. Song, High-pressure melting of tantalum from the modified Z method, *J. Appl. Phys.* 114 (2013) 163514.
- [57] N.Q. Hoc, T.D. Cuong, B.D. Tinh, L.H. Viet, High-pressure melting curves of FCC metals Ni, Pd and Pt with defects, *Mod. Phys. Lett. B* 33 (2019) 1950300.
- [58] P.M. Agrawal, B.M. Rice, D.L. Thompson, Molecular dynamics study of the effects of voids and pressure in defect-nucleated melting simulations, *J. Chem. Phys.* 118 (2003) 9680–9688.
- [59] Y. Zou, S. Xiang, C. Dai, Investigation on the efficiency and accuracy of methods for calculating melting temperature by molecular dynamics simulation, *Comput. Mater. Sci.* 171 (2020) 109156.
- [60] C. Cazorla, D. Errandonea, High-Pressure, High-Temperature Phase Diagram of Calcium Fluoride from Classical Atomistic Simulations, *J. Phys. Chem. C* 117 (2013) 11292–11301.
- [61] V.S. Dozhdikov, A.Y. Basharin, P.R. Levashov, Two-phase simulation of the crystalline silicon melting line at pressures from -1 to 3 GPa, *J. Chem. Phys.* 137 (2012) 054502.
- [62] Z.-Y. Zeng, C.-E. Hu, L.-C. Cai, X.-R. Chen, F.-Q. Jing, Molecular dynamics study of the melting curve of NiTi alloy under pressure, *J. Appl. Phys.* 109 (2011) 043503.
- [63] Y.N. Wu, L.P. Wang, Y.S. Huang, D.M. Wang, Melting of copper under high pressures by molecular dynamics simulation, *Chem. Phys. Lett.* 515 (2011) 217–220.
- [64] N.S. Weingarten, W.D. Mattson, B.M. Rice, Determination of the pressure dependent melting temperatures of Al and Ni using molecular dynamics, *J. Appl. Phys.* 106 (2009) 063524.
- [65] E.G. Noya, C. Vega, E. de Miguel, Determination of the melting point of hard spheres from direct coexistence simulation methods, *J. Chem. Phys.* 128 (2008) 154507.
- [66] S. Yoo, X.C. Zeng, J.R. Morris, The melting lines of model silicon calculated from coexisting solid-liquid phases, *J. Chem. Phys.* 120 (2004) 1654–1656.
- [67] K. Li, R. Khanna, J. Zhang, G. Li, H. Li, C. Jiang, M. Sun, Z. Wang, Y. Bu, M. Bouhadja, Z. Liu, M. Barati, Determination of the accuracy and reliability of molecular dynamics simulations in estimating the melting point of iron: Roles of interaction potentials and initial system configurations, *J. Mol. Liq.* 290 (2019) 111204.
- [68] K. Rybacki, S. Winczewski, V. Plechystyy, J. Rybicki, Improvements to the two-phase sandwich method for calculating the melting points of pure metals, *Comput. Methods, Sci. Technol.* 25 (2019) 105–116.
- [69] A.N. Singh, J.C. Dyre, U.R. Pedersen, Solid-liquid coexistence of neon, argon, krypton, and xenon studied by simulations, *J. Chem. Phys.* 154 (2021) 134501.
- [70] R.S. DeFever, H. Wang, Y. Zhang, E.J. Maginn, Melting points of alkali chlorides evaluated for a polarizable and non-polarizable model, *J. Chem. Phys.* 153 (2020) 011101.
- [71] C. Cazorla, A.K. Sagotra, M. King, D. Errandonea, High-Pressure Phase Diagram and Superionicity of Alkaline Earth Metal Difluorides, *J. Phys. Chem. C* 122 (2018) 1267–1279.

- [72] L.-F. Zhu, B. Grabowski, J. Neugebauer, Efficient approach to compute melting properties fully from *ab initio* with application to Cu, Phys. Rev. B 96 (2017) 224202.
- [73] W.-J. Zhang, Z.-Y. Liu, Z.-L. Liu, L.-C. Cai, Melting curves and entropy of melting of iron under Earth's core conditions, Phys. Earth Planet. In. 244 (2015) 69–77.
- [74] E. Asadi, M. Asle Zaeem, S. Nouranian, M.I. Baskes, Two-phase solid-liquid coexistence of Ni, Cu, and Al by molecular dynamics simulations using the modified embedded-atom method, Acta Mater. 86 (2015) 169–181.
- [75] T. Inagaki, T. Ishida, Free energy based melting point prediction by NVT simulation with solid-liquid two-phase configuration, Chem. Phys. Lett. 662 (2016) 273–279.
- [76] D.M. Eike, J.F. Brennecke, E.J. Maginn, Toward a robust and general molecular simulation method for computing solid-liquid coexistence, J. Chem. Phys. 122 (2005) 014115.
- [77] G. Grochola, Constrained fluid λ -integration: Constructing a reversible thermodynamic path between the solid and liquid state, J. Chem. Phys. 120 (2004) 2122–2126.
- [78] D. Frenkel, A.J. Ladd, New Monte Carlo method to compute the free energy of arbitrary solids. Application to the fcc and hcp phases of hard spheres, J. Chem. Phys. 81 (1984) 3188–3193.
- [79] W.G. Hoover, F.H. Ree, Use of computer experiments to locate the melting transition and calculate the entropy in the solid phase, J. Chem. Phys. 47 (1967) 4873–4878.
- [80] U.R. Pedersen, F. Hummel, G. Kresse, G. Kahl, C. Dellago, Computing Gibbs free energy differences by interface pinning, Phys. Rev. B 88 (2013) 094101.
- [81] E.J. Meijer, D. Frenkel, R.A. LeSar, A.J.C. Ladd, Location of melting point at 300 K of nitrogen by Monte Carlo simulation, J. Chem. Phys. 92 (1990) 7570–7575.
- [82] B.J. Jesson, P.A. Madden, *Ab initio* determination of the melting point of aluminum by thermodynamic integration, J. Chem. Phys. 113 (2000) 5924–5934.
- [83] J. Anwar, D. Frenkel, M.G. Noro, Calculation of the melting point of NaCl by molecular simulation, J. Chem. Phys. 118 (2003) 728–735.
- [84] F. Colonna, J.H. Los, A. Fasolino, E.J. Meijer, Properties of graphite at melting from multilayer thermodynamic integration, Phys. Rev. B 80 (2009) 134103.
- [85] T. Taniuchi, T. Tsuchiya, The melting points of MgO up to 4 TPa predicted based on *ab initio* thermodynamic integration molecular dynamics, J. Phys.: Condens. Matter 30 (2018) 114003.
- [86] J. Luo, Y. Cheng, C. Zhou, T. Sinno, L. Liu, A general approach for calculating melt-solid impurity segregation coefficients based on thermodynamic integration, J. Appl. Phys. 130 (2021) 025702.
- [87] T. Miryashkin, O. Klimanova, V. Ladygin, A. Shapeev, Bayesian inference of composition-dependent phase diagrams, Phys. Rev. B 108 (2023) 174103.
- [88] Y. Zhang, E.J. Maginn, A comparison of methods for melting point calculation using molecular dynamics simulations, J. Chem. Phys. 136 (2012) 144116.
- [89] S. Cajahuringa, A. Antonelli, Non-equilibrium free-energy calculation of phase-boundaries using LAMMPS, Comput. Mater. Sci. 207 (2022) 111275.
- [90] K. Fuchizaki, K. Okamoto, Determination of a melting curve using the one-phase approach, Phys. Lett. A 380 (2016) 293–298.
- [91] Q.-J. Hong, A. van de Walle, A user guide for SLUSCHI: Solid and Liquid in Ultra Small Coexistence with Hovering Interfaces, Calphad 52 (2016) 88–97.
- [92] R. Freitas, M. Asta, M. de Koning, Nonequilibrium free-energy calculation of solids using LAMMPS, Comput. Mater. Sci. 112 (2016) 333–341.
- [93] Q.J. Hong, A. van de Walle, Solid-liquid coexistence in small systems: A statistical method to calculate melting temperatures, J. Chem. Phys. 139 (2013) 094114.
- [94] J. Ma, W. Li, G. Yang, S. Zheng, Y. He, X. Zhang, X. Zhang, Modeling the pressure-dependent melting temperature of metals, Phys. Earth Planet. In. 309 (2020) 106602.
- [95] O. Klimanova, T. Miryashkin, A. Shapeev, Accurate melting point prediction through autonomous physics-informed learning, Phys. Rev. B 108 (2023) 184103.
- [96] G. Pilania, J.E. Gubernatis, T. Lookman, Structure classification and melting temperature prediction in octet AB solids via machine learning, Phys. Rev. B 91 (2015) 214302.
- [97] R. Jinnochi, F. Karsai, G. Kresse, On-the-fly machine learning force field generation: Application to melting points, Phys. Rev. B 100 (2019) 014105.
- [98] D. Marchand, A. Jain, A. Glensk, W.A. Curtin, Machine learning for metallurgy I. A neural-network potential for Al-Cu, Phys. Rev. Mater. 4 (2020) 103601.
- [99] Z. Wei, J. Yu, Y. Lu, J. Han, C. Wang, X. Liu, Prediction of diffusion coefficients in fcc, bcc and hcp phases remained stable or metastable by the machine-learning methods, Mater. Des. 198 (2021) 109287.
- [100] Q.-J. Honga, S.V. Ushakov, A. van de Walle, A. Navrotsky, Melting temperature prediction using a graph neural network model: From ancient minerals to new materials, Proc. Natl. Acad. Sci. 119 (2022) e2209630119.
- [101] R.E. Rytsev, N.M. Chitchelkatchev, Deep machine learning potentials for multicomponent metallic melts: development, predictability and compositional transferability, J. Mol. Liq. 349 (2022) 118181.
- [102] R. Zhao, S. Wang, Z. Kong, Y. Xu, K. Fu, P. Peng, C. Wu, Development of a neuroevolution machine learning potential of Pd-Cu-Ni-P alloys, Mater. Des. 231 (2023) 112012.
- [103] A.O. Tipeev, R.E. Rytsev, N.M. Chitchelkatchev, S. Ramprakash, E.D. Zanotto, Machine learning-assisted MD simulation of melting in superheated AlCu validates the Classical Nucleation Theory, J. Mol. Liq. 387 (2023) 122606.
- [104] N. Joshi, N. Mathur, T. Mane, D. Sundaram, Size effect on melting temperatures of alumina nanocrystals: Molecular dynamics simulations and thermodynamic modeling, Comput. Mater. Sci. 145 (2018) 140–153.
- [105] A.B. Belonoshko, T. Lukinov, L. Burakovskiy, D.L. Preston, A. Rosengren, Melting of a polycrystalline material: Melting of real materials, Eur. Phys. J. Spec. Top. 216 (2013) 199–204.
- [106] M.P. Hazarika, S.N. Chakraborty, Study of structural stability of copper crystal with voids from molecular dynamics simulations, Chem. Phys. Lett. 730 (2019) 521–526.
- [107] M. KaczmarSKI, O.N. Bedoya-Martinez, E.R. Hernández, Phase diagram of silicon from atomistic simulations, Phys. Rev. Lett. 94 (2005) 095701.
- [108] D. Alfè, G. Price, M. Gillan, Iron under Earth's core conditions: Liquid-state thermodynamics and high-pressure melting curve from *ab initio* calculations, Phys. Rev. B 65 (2002) 165118.
- [109] K. Dang, J. Chen, B. Rodgers, S. Fensin, Lava., 1.0: A general-purpose python toolkit for calculation of material properties with LAMMPS and VASP, Comput. Phys. Commun. 286 (2023) 108667.
- [110] L.-F. Zhu, J. Janssen, S. Ishibashi, F. Körmann, B. Grabowski, J. Neugebauer, A fully automated approach to calculate the melting temperature of elemental crystals, Comput. Mater. Sci. 187 (2021) 110065.
- [111] G. Hu, C. Luo, L. Wu, Q. Tang, Z. Ren, B. Xu, Molecular dynamics simulation of solid/liquid interfacial energy of uranium, J. Nucl. Mater. 538 (2020) 152183.
- [112] J. Wang, S. Yoo, J. Bai, J.R. Morris, X.C. Zeng, Melting temperature of ice Ih calculated from coexisting solid-liquid phases, J. Chem. Phys. 123 (2005) 36101.
- [113] S. Plimpton, Fast parallel algorithms for short-range molecular dynamics, J. Comput. Phys. 117 (1995) 1–19.
- [114] Y. Mishin, M. Mehl, D. Papaconstantopoulos, A. Voter, J. Kress, Structural stability and lattice defects in copper: *Ab initio*, tight-binding, and embedded-atom calculations, Phys. Rev. B 63 (2001) 224106.
- [115] A. Stukowski, Visualization and analysis of atomistic simulation data with OVITO—the Open Visualization Tool, Model. Simul. Mater. Sci. Eng. 18 (2009) 015012.
- [116] Z. Song, W. Luo, X. Fan, Y. Zhu, Atomic fast dynamic motion on the Cu nanoparticle's surface before melting: A molecular dynamics study, Appl. Surf. Sci. 606 (2022) 154901.
- [117] T. Karabacak, J.S. DeLuca, P.-I. Wang, G.A. Ten Eyck, D. Ye, G.-C. Wang, T.-M. Lu, Low temperature melting of copper nanorod arrays, J. Chem. Phys. 99 (2006) 064304.
- [118] S. Safaltn, S. Gürmen, Molecular dynamics simulation of size, temperature, heating and cooling rates on structural formation of Ag-Cu-Ni ternary nanoparticles ($Ag_{34}Cu_{33}Ni_{33}$), Comput. Mater. Sci. 183 (2020) 109842.
- [119] R. Essajai, A. Rachadi, E. Feddi, N. hassanain, MD simulation-based study on the thermodynamic, structural and liquid properties of gold nanostructures, Mater. Chem. Phys. 218 (2018) 116–121.
- [120] Q. Zhang, J. Wang, S. Tang, Y. Wang, J. Li, W. Zhou, Z. Wang, Molecular dynamics investigation of the local structure in iron melts and its role in crystal nucleation during rapid solidification, Phys. Chem. Chem. Phys. 21 (2019) 4122–4135.
- [121] J. Xu, M. Xiang, B. Dang, Z. Jian, Relation of cooling rate, undercooling and structure for rapid solidification of iron melt, Comput. Mater. Sci. 128 (2017) 98–102.
- [122] P.M. Larsen, S. Schmidt, J. Schiøtz, Robust structural identification via polyhedral template matching, Model. Simul. Mater. Sci. Eng. 24 (2016) 055007.
- [123] A.M. Goryaeva, C. Fusco, M. Bugnet, J. Amodeo, Influence of an amorphous surface layer on the mechanical properties of metallic nanoparticles under compression, Phys. Rev. Mater. 3 (2019) 033606.
- [124] X.H. Yi, R.S. Liu, Z.A. Tian, Z.Y. Hou, X.Y. Li, Q.Y. Zhou, Formation and evolution properties of clusters in liquid metal copper during rapid cooling processes, T. Nonferr. Metal. Soc. 18 (2008) 33–39.
- [125] S. Becker, E. Devijver, R. Molinier, N. Jakse, Glass-forming ability of elemental zirconium, Phys. Rev. B 102 (2020) 104205.
- [126] Y. Du, Z. Meng, Q. Yan, C. Wang, Y. Tian, W. Duan, P. Lin, Deep potential for a face-centered cubic Cu system at finite temperatures, Phys. Chem. Chem. Phys. 24 (2022) 18361–18369.
- [127] D. Turnbull, Formation of crystal nuclei in liquid metals, J. Appl. Phys. 21 (1950) 1022–1028.
- [128] H. Jones, The solid-liquid interfacial energy of metals: calculations versus measurements, Mater. Lett. 53 (2002) 364–366.
- [129] C. Ronchi, M. Sheindlin, Melting point of MgO, J. Appl. Phys. 90 (2001) 3325–3331.
- [130] R.H. Lamoreaux, D.L. Hildenbrand, L. Brewer, High-Temperature Vaporization Behavior of Oxides II. Oxides of Be, Mg, Ca, Sr, Ba, B, Al, Ga, In, Tl, Si, Ge, Sn, Pb, Zn, Cd, and Hg, J. Phys. Chem. Ref. Data 16 (1987) 419–443.
- [131] T.D. Cuong, A.D. Phan, Theoretical model for the high-pressure melting process of MgO with the B1 structure, Vacuum 189 (2021) 110231.
- [132] S. Wang, Z. Fan, R.S. Koster, C. Fang, M.A. van Huis, A.O. Yalcin, F.D. Tichelaar, H.W. Zandbergen, T.J.H. Vlugt, New *Ab Initio* Based Pair Potential for Accurate Simulation of Phase Transitions in ZnO, J. Phys. Chem. C 118 (2014) 11050–11061.
- [133] A.K. Sagotra, C. Cazorla, Stress-Mediated Enhancement of Ionic Conductivity in Fast-Ion Conductors, ACS Appl. Mater. Interfaces 9 (2017) 38773–38783.
- [134] X. Wang, Y. Wang, J. Wang, S. Pan, Q. Lu, H.T. Wang, D. Xing, J. Sun, Pressure Stabilized Lithium-Aluminum Compounds with Both Superconducting and Superionic Behaviors, Phys. Rev. Lett. 129 (2022) 246403.